Advanced Healthcare Materials

ADVANCED HEALTHCARE MATERIALS
www.advhealthmat.de

RESEARCH ARTICLE OPEN ACCESS

Tumor-Targeted Hyaluronic Acid/Tannic Acid-Engineered Oxygen Nanogenerators With IR780 Payloads Enable Dual-Mode Glutathione Depletion and Effective Singlet Oxygen Generation for Melanoma Treatment

Chai-How Hsu[1] | I-Ju Liu[1] | Hsiang-Yun Chih[1] | Tsai-Ching Hsu[2,3,4] | Ju-An Liang[2] | Chia-Wei Kuo[2] | Bor-Show Tzang[2,3,4,5] | Wen-Hsuan Chiang[1,6]

[1]Department of Chemical Engineering, National Chung Hsing University, Taichung, Taiwan | [2]Institute of Medicine, Chung Shan Medical University, Taichung, Taiwan | [3]Immunology Research Center, Chung Shan Medical University, Taichung, Taiwan | [4]Department of Clinical Laboratory, Chung Shan Medical University Hospital, Taichung, Taiwan | [5]Department of Biochemistry, School of Medicine, Chung Shan Medical University, Taichung, Taiwan | [6]i-Center for Advanced Science and Technology (iCAST), National Chung Hsing University, Taichung, Taiwan

Correspondence: Bor-Show Tzang (bstzang@csmu.edu.tw) | Wen-Hsuan Chiang (whchiang@dragon.nchu.edu.tw)

Received: 12 February 2026 | **Revised:** 14 July 2026 | **Accepted:** 7 August 2026

Keywords: dual-mode GSH consumption | hyaluronic acid | tumor-targeting oxygen nanogenerators

ABSTRACT

Despite advances in combined photothermal (PTT) and photodynamic (PDT) therapy for melanoma, therapeutic efficacy remains limited by tumor hypoxia, intracellular glutathione (GSH), insufficient tumor targeting, and photobleaching of photosensitizers. Herein, tumor-targeting and GSH self-depleting hyaluronic acid (HA)/tannic acid (TA)-engineered Prussian blue (PB) oxygen nanogenerators (ONs) loaded with IR780 (IHTPB ONs) are developed to enhance synergistic PTT/PDT. The IHTPB ONs exhibit uniform morphology, excellent colloidal stability, acidity/GSH-responsive IR780 release, high photothermal conversion efficiency (60%), and outstanding photothermal stability. Importantly, PB-mediated GSH oxidation and TA-mediated GSH conjugation enable dual-mode GSH depletion, while PB catalyzes oxygen generation to alleviate tumor hypoxia and promote IR780-mediated singlet oxygen production. Following CD44-mediated cellular uptake, IHTPB ONs effectively deplete intracellular GSH and, under near-infrared irradiation, induce robust reactive oxygen species generation and hyperthermia, leading to mitochondrial dysfunction, lipid peroxidation, apoptosis, and ferroptosis. In vivo, IHTPB ONs exhibit superior tumor accumulation and significantly enhanced antitumor efficacy compared with free IR780 and non-targeted nanoparticles, resulting in prolonged survival of melanoma-bearing mice. This work provides an effective nanoplatform integrating tumor targeting, oxygen self-supply, and dual-mode GSH depletion to potentiate synergistic PTT/PDT for melanoma therapy.

1 | Introduction

Melanoma, or malignant melanoma, is a cancerous tumor originating from melanocytes, most commonly found in the skin [1–3]. Despite representing only 6.8% of all skin malignancies, it is highly lethal, responsible for approximately 75% of skin cancer-related deaths [1]. Regardless of intensive research and clinical efforts in the past decades, melanoma remains one of the deadliest cancers, characterized by its aggressive, unpredictable nature, and persistently high mortality worldwide [1–5]. Surgery remains the primary treatment for most melanomas, while stage III–IV patients are typically managed with immunotherapy, targeted

therapy, or radiotherapy [2, 6–8]. Chemotherapy may benefit select patients with stage IV melanoma after failure of other treatments [2]. However, melanoma shows strong resistance to chemotherapy and radiotherapy and carries a high risk of recurrence after surgery [9]. Recently, immunotherapy using monoclonal antibodies targeting immune checkpoint proteins has shown significant progress in eliciting durable and effective immune responses for advanced melanoma. Nevertheless, many patients still experience limited or no benefit from these treatments [10–12]. Thus, effective strategies are urgently needed to eliminate primary melanoma and residual cells, thereby preventing metastasis and recurrence.

Phototherapy, encompassing photothermal (PTT) and photodynamic therapy (PDT), is a non-invasive and effective approach for treating superficial tumors [13–15], and has gained considerable attention for its ability to offer precise spatial selectivity with minimal invasiveness. PDT employs photosensitizers (PS) activated by specific wavelengths of light to generate reactive oxygen species (ROS) that destroy target cells or tissues [13, 16, 17]. However, accumulating evidence indicates that PDT alone exhibits limited efficacy against melanoma, primarily due to the restricted tissue penetration of laser light, particularly in advanced metastatic disease, as well as the hypoxic tumor microenvironment [2, 17, 18]. In contrast to PDT, PTT uses PS to convert light energy into heat, inducing localized hyperthermia to damage cancer cells [17, 19, 20]. Nevertheless, PTT alone is insufficient to achieve complete tumor ablation because of limited light penetration and heterogeneous heat distribution, which can result in residual tumor cells and subsequent relapse and metastasis [21, 22]. To overcome the limitations of single PDT or PTT, combining PDT with PTT has been shown to produce synchronous and synergistic antitumor effects by alleviating tumor hypoxia driven by photothermal-enhanced blood flow [2, 13, 22]. Furthermore, PTT- and PDT-induced antitumor immune effects in the tumor microenvironment by promoting local immunogenic cell death (ICD) [23–25]. For example, Tao's group fabricated adjuvant monophosphoryl lipid A (MPLA) lipid bilayer-enveloped and photosensitizer indocyanine green (ICG)-loaded gold nanocages (MLI-AuNCs) for immunogenic phototherapy of aggressive melanoma [5]. The MLI-AuNCs showed remarkable tumor accumulation and exerted robust PTT/PDT effects to eradicate primary tumors under a single near-infrared (NIR) irradiation, while simultaneously triggering a strong antitumor immune response to suppress metastasis and recurrence. Moreover, Liu and colleagues designed INEs, an innovative ethosome co-loaded with the photosensitizer IR251 and the indoleamine-2,3-dioxygenase (IDO) inhibitor NLG919 [1]. INEs represent a promising strategy for melanoma treatment by a combination of phototherapy and immunotherapy with high safety. Despite some progress in the use of the combination of PTT and PDT for melanoma treatment, the efficacy of phototherapy against advanced and metastatic tumors remains poor due to tumor hypoxia, ROS depletion in elevated intracellular glutathione (GSH) levels, insufficient tumor targeting, the low photothermal conversion efficiency, and severe photobleaching of small-molecule photosensitizers [26–28]. To alleviate hypoxia in tumors for improved PDT efficacy, catalase-like nanoparticles capable of generating O_2 within the tumor microenvironment through catalyzing reactions have been extensively developed [28–31]. Prussian blue (PB) nanoparticles, composed of Fe^{2+} and Fe^{3+} ions coordinated with cyanide, have been recognized as oxygen nanogenerators (ONs) capable of decomposing endogenous hydrogen peroxide (H_2O_2) to O_2, which is advantageous in PDT [32–34]. Also, several studies report that PB nanoparticles can convert NIR light into heat and be used as a PTT reagent to ablate tumors [35, 36]. Notably, due to excellent biocompatibility, PB has been approved by the US Food and Drug Administration (FDA) for use as an antidote for heavy metal poisoning and its inclusion in the World Health Organization (WHO) essential medicines catalog [32, 37]. On the other hand, to decline the ability of tumor cells to scavenge ROS, some advanced therapeutic nanoparticles were equipped with endogenous GSH-depleting capability, thus enhancing ROS-based anticancer effect [38–40]. Tannic acid (TA), a naturally occurring polyphenol, possesses abundant phenolic hydroxyl groups that enable hydrogen bonding and metal-phenolic coordination with various biomolecules, polymers, and metal ions [41, 42]. These characteristics have facilitated the development of multifunctional nanoplatforms for drug delivery and cancer therapy. In addition, oxidized tannic acid can generate electrophilic quinone-like species capable of reacting with nucleophilic thiols such as GSH or cysteine, leading to the formation of covalent thiol-polyphenol adducts via Michael addition-type reactions [43]. Hyaluronic acid (HA) is a natural polysaccharide consisting of repeating disaccharide units of D-glucuronic acid and *N*-acetyl-D-glucosamine linked via $\beta(1\rightarrow3)$ glycosidic bonds. Owing to its excellent biocompatibility, hydrophilicity, water solubility, low immunogenicity, and abundant reactive functional groups for chemical modification, HA has been widely employed as a versatile biomaterial [44, 45]. In addition, HA has been extensively functionalized on the surface of nanocarriers for tumor-targeted drug delivery, as it can specifically bind to CD44 receptors, which are overexpressed on the membranes of various cancer cells [44, 45].

In light of the aforementioned challenges in melanoma phototherapy, we designed tumor-targeting and GSH self-depleting HA/TA-modified PB ONs as carriers for the IR780 photosensitizer to maximize the therapeutic efficacy of combined PTT and PDT (Scheme 1a). Through the coordination between TA molecules and Fe^{2+}/Fe^{3+} ions of PB ONs, the TA-coated PB (TPB) ONs were attained. Subsequently, the cationic IR780 molecules were loaded into the TPB ONs through π–π stacking, electrostatic attraction, and hydrogen bonding between the IR780 molecules and the TA-enriched surfaces. The IR780-loaded TPB (ITPB) ONs were further decorated with thiol-modified HA (HA-SH) to attain IR780-loaded HA-coated TPB (IHTPB) ONs. The IHTPB ONs not only exhibited a uniform cubic shape, stable colloidal suspension, and acidity/GSH-enhanced IR780 liberation but also displayed prominent photothermal conversion efficiency (60%) and stability, PB-facilitated O_2 generation, and IR780-driven $^1O_2$-producing capability. Importantly, the IHTPB ONs achieved dual-mode GSH depletion via PB-mediated oxidation and photothermal-enhanced TA-driven Michael addition. After CD44-mediated endocytosis by B16F10 melanoma cells, IHTPB ONs effectively depleted intracellular GSH, generated sufficient O_2, and, upon 808 nm NIR laser irradiation, produced both $^1O_2$ and hyperthermia. These effects induced mitochondrial damage and lipid peroxidation (LPO), ultimately triggering apoptosis and ferroptosis. Notably, compared to the ITPB ONs (without HA decoration) and free IR780 molecules, the tumor-targeting IHTPB

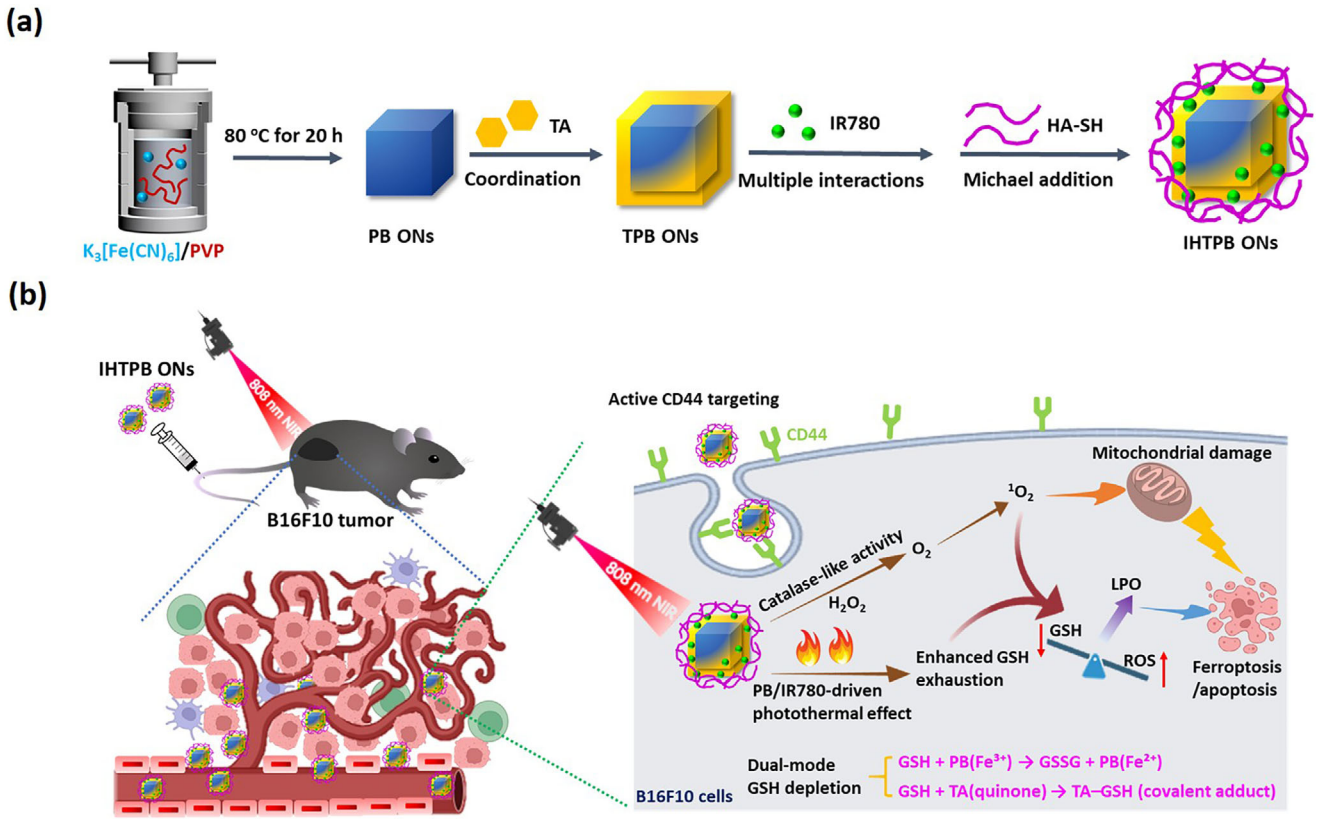

SCHEME 1 | Schematic design of (a) fabrication of IHTPB ONs and (b) their PTT/PDT-mediated antitumor effects.

ONs markedly inhibited B16F10 tumor growth and prolonged mouse survival by the self-depleting GSH and self-producing O_2-enhanced PTT/PDT-mediated anticancer effects combined with ferroptosis (Scheme 1b). To the best of our knowledge, different from most of the PB nanoparticles decorated with HA segments alone [33, 34], the surfaces of PB ONs engineered with both TA and HA in this work achieved dual-mode GSH depletion and enhanced photothermal stability of photosensitizer to augment melanoma-targeted synergistic PTT/PDT therapy.

2 | Experimental Section

2.1 | Materials and Reagents

HA-SH segments were synthesized using the previously reported method [45], and their chemical composition was characterized by ^{1}H-NMR (Figure S1). The HA (Mw 30–50 kDa) was purchased from Glentham Life Science (UK). Potassium hexacyanoferrate(III) (≥99%), IR780 (≥95%), propidium iodide (PI), 2',7'-dichlorodihydrofluorescein diacetate (DCFH-DA), 3-(4,5-dimethylthiazol-2-yl)-2,5-diphenyltetrazolium bromide (MTT), 1,3-diphenylisobenzofuran (DPBF), and Dulbecco's modified Eagle's medium-high glucose were obtained from Sigma-Aldrich (USA). Poly(vinylpyrrolidone) (PVP) K15 (Mw 10 kDa) was supplied by Tokyo Chemical Industry Co., Ltd., and TA (95%) was purchased from Acros Organics. 5,5′-Dithiobis (2-nitrobenzoic acid) (DTNB, 99%) was purchased from Fluorochem (UK). Fetal bovine serum (FBS) was purchased from Hyclone (USA). Hoechst 33342 was purchased from Invitrogen. $[Ru(dpp)_3]Cl_2$ was obtained from Alfa-Aesar Co. Ltd. The JC-1 assay kit was purchased from MedChemExpress (USA). Calcein-AM was obtained from AAT Bioquest (USA). BODIPY 581/591 C11 was obtained from Thermo Fisher Scientific (USA). Anti-Ki67 antibodies (no ab15580), antiglutathione peroxidase 4 (GPX4) antibodies (no ab125066), and anti-HIF-1α antibodies were purchased from Abcam. All other chemicals were reagent grade and used as received. B16F10 cells (murine skin melanoma cell line) and CT26 (murine colon cancer cell line) were acquired from the Food Industry Research and Development Institute (Hsinchu City, Taiwan).

2.2 | Preparation of PB ONs and TPB ONs

First, $K_3Fe(CN)_6$ (33 mg) and PVP (750 mg) were co-dissolved in a mixed solution of ethanol (95%, 4.5 mL) and aqueous HCl (1 M, 5.5 mL). The resulting solution was then transferred into a Teflon-lined autoclave and maintained at 80°C in an oven for 20 h. After the reaction, the obtained product was centrifuged (16 000 rpm, 10 min) and washed once with water and ethanol. Finally, the PB ONs were dispersed in deionized water and stored at 4°C for future use. The TPB ONs were prepared with the following approach. TA aqueous solution (40 mg/mL, 0.12 mL) was added dropwise to PB ON solution (1 mg/mL, 1 mL) and stirred at room temperature for 30 min. The resulting mixture was then centrifuged (16 000 rpm, 10 min) and washed once with deionized water. Finally, the product was dispersed in deionized water and stored at 4°C for future use.

2.3 | Preparation of IHTPB ONs

An IR780 solution (2 mg/mL, 0.1 mL) was added dropwise to a TPB solution (1.2 mg/mL, 1 mL) and stirred at room temperature for 2 h. Subsequently, an HA-SH solution (0.5 mg/mL, 1 mL) was introduced dropwise into the mixture and stirred for an additional 24 h. The resulting dispersion was centrifuged (16 000 rpm, 10 min) and washed once with water. The final product was dispersed in deionized water and stored at 4°C for further use. For comparison, ITPB ONs and HTPB ONs were prepared using the same procedure.

2.4 | Characterization

X-ray diffraction (XRD) patterns of the various PB-based ONs were obtained using a D8 Discover x-ray diffractometer (Bruker, Germany). The particle size, size distribution, and zeta potential of the PB-based ONs in aqueous solution were measured using a Litesizer 500 (Anton Paar, USA). The morphology of the PB-containing ONs was examined by scanning electron microscopy (SEM; JSM-7800F, JEOL, Japan) and transmission electron microscopy (TEM; JEM-1400, JEOL, Japan). X-ray energy-dispersive spectroscopy (EDS) elemental mapping of IHTPB ONs was performed using TEM (JEM-F200, JEOL, Japan). UV–Vis absorption spectra of IR780, TA, PB ONs, TPB ONs, and IHTPB ONs in a pH 7.4 aqueous solution were recorded with a UV–vis spectrophotometer (U2900, HITACHI). Fourier-transform infrared (FT-IR) spectra were acquired using an FT-IR spectrometer (FT-720, HORIBA, Japan). Thermogravimetric analysis (TGA) was conducted under a nitrogen atmosphere using a thermogravimetric analyzer (EXSTAR TG/DTA 6200, Seiko Instruments Inc.). X-ray photoelectron spectroscopy (XPS) analysis of PB, HTPB, ITPB, and IHTPB ONs was conducted using an x-ray photoelectron spectrometer (PHI 5000 VersaProbe III, ULVAC, Japan).

2.5 | Determination of TA Adsorption Content and IR780 Loading Content

To quantify TA adsorption content and IR780 loading content, various PB-based ON solutions were centrifuged, and the absorbance of the supernatant at 275 nm (for TA) and 785 nm (for IR780) was measured using a UV–vis spectrophotometer. The calibration curves used for TA adsorption and IR780 loading content determination were established by the absorbance of TA and IR780 with different concentrations in deionized water. The following formulas were used to estimate the TA adsorption content (AC), IR780 loading efficiency (LE), and loading content (LC).

$$\mathrm{AC}\ (\%) = \frac{[\text{Weight of TA in feed} - \text{weight of TA in the supernatant}]}{\text{Total weight of TA} - \text{coated ONs}} \times 100\%$$

$$\mathrm{LE}\ (\%) = \frac{[\text{Weight of IR780 in feed} - \text{weight of IR780 in the supernatant}]}{\text{Weight of IR780 in feed}} \times 100\%$$

$$\mathrm{LC}\ (\%) = \frac{[\text{Weight of IR780 in feed} - \text{weight of IR780 in the supernatant}]}{\text{Total weight of IR780} - \text{loaded ONs}} \times 100\%$$

2.6 | Photothermal Conversion Effect

Free IR780, PB ONs, ITPB ONs, and IHTPB ONs were each dispersed in 1.0 mL of deionized water and exposed to 808 nm NIR laser irradiation (1.0 W/cm^2) for 3 min. In all experiments, the concentrations of PB ONs and IR780 were fixed at 50 and 9 μg/mL, respectively. During irradiation, the solution temperatures and corresponding thermal images were recorded using an infrared thermal imaging camera (Thermo Shot F20, NEC Avio Infrared Technologies, Germany). In addition, temperature increases of aqueous IHTPB ON solutions at different concentrations under 808 nm laser irradiation (1.0 W/cm^2), as well as of IHTPB ONs dispersions (31.6 μg/mL) subjected to varying laser power densities, were measured using the same instrument.

To evaluate the photothermal conversion efficiency (η) of IHTPB ONs, the solution was irradiated with an 808 nm laser for 5 min and then allowed to cool to room temperature. The temperature variation during this process was recorded using a thermal imaging camera, and the photothermal conversion efficiency was calculated according to previously reported equations [16, 46]. For comparison, the photothermal conversion efficiencies of free IR780 and PB ONs were determined using the same procedure. To evaluate photothermal stability, aqueous solutions containing free IR780, ITPB ONs, and IHTPB ONs (IR780 concentration: 9 μg/mL) were subjected to 808 nm laser irradiation (1.0 W/cm^2) with 1.5 min laser on and 3 min laser off for three cycles, while the solution temperature was monitored using an infrared thermal imaging camera. For comparison, an aqueous PB ONs solution (50 μg/mL) was treated under identical conditions. In addition, during the repeated laser on/off cycles, the UV–vis absorption spectra of free IR780 and IHTPB ON solutions in the range of 500–900 nm were recorded using a UV–vis spectrophotometer.

2.7 | In Vitro IR780 Liberation

The in vitro IR780 release of IHTPB ONs was evaluated using the following approach. First, IHTPB ONs were dispersed in pH 7.4 PBS and pH 5.0 acetate buffer, with or without 10 mM GSH, respectively, at 37°C. A small amount of Tween 80 was added to the above solutions to prevent precipitation of the hydrophobic IR780 molecules released from the IHTPB ONs, thereby facilitating accurate analysis. At predetermined time intervals, the dispersion was centrifuged at 16 000 rpm for 20 min. The absorbance of the supernatant at 785 nm was then measured using a UV–vis spectrophotometer to determine the amount of IR780 released from the IHTPB ONs.

2.8 | PB/TA-Elicited GSH Depletion

The GSH-depleting capability of TA molecules, PB ONs, HTPB ONs, and IHTPB ONs was evaluated using a DTNB assay. Each

sample was dispersed in 1 mL of a 75 μM GSH aqueous solution (pH 7.4) at defined concentrations (TA: 10 μg/mL; PB: 50 μg/mL) and incubated at 37 or 50°C for 2, 4, and 6 h. After incubation, the mixtures were centrifuged at 16 000 rpm for 10 min, and the supernatants were reacted with 0.1 mL of DTNB solution (1 mM) for 10 min. The absorbance of the generated TNB was subsequently recorded over the wavelength range of 380–550 nm.

2.9 | O_2-Generating Capacity

The PB ONs and IHTPB ONs of different concentrations were dispersed in a 10 mM H_2O_2-containing aqueous solution, and the O_2 level of the mixture was monitored for 5 min with a dissolved oxygen meter (PL-700PD, MADO, Taiwan). The O_2 concentration of pure water and H_2O_2 solutions was also determined under the same conditions for comparison.

2.10 | NIR-Triggered $^1O_2$ Production

DPBF was employed as a $^1O_2$-sensitive indicator to evaluate the $^1O_2$ generation capability of IHTPB ONs under NIR laser irradiation. Free IR780 or IHTPB ONs (IR780 concentration: 9 μg/mL) were dispersed in 1 mL of an aqueous DPBF solution (50 μg/mL) and subjected to NIR laser irradiation (808 nm, 1 W/cm^2) for 1, 2, and 3 min. Subsequently, the absorption spectra of the resulting solutions in the range of 380–900 nm were recorded using a UV–vis spectrophotometer (U2900, Hitachi, Japan). For comparison, changes in DPBF absorption in an HTPB ON solution (70 μg/mL) were measured under identical conditions. In addition, to investigate the influence of H_2O_2 and GSH on the $^1O_2$-generating capability of IHTPB ONs, DPBF absorption was measured after NIR laser irradiation for various durations in IHTPB ON or free IR780 solutions (IR780 concentration = 9 μg/mL) containing 10 mM H_2O_2, or a combination of 10 mM H_2O_2 and 1 mM GSH, respectively.

2.11 | In Vitro Cellular Uptake, Intracellular GSH Depletion, O_2, and ROS Generation

The CD44-targeting capability of IHTPB ONs was evaluated using CD44-overexpressing B16F10 cells as a model. B16F10 cells (2×10^5 cells/well) were seeded on round glass coverslips in 6-well plates and incubated with ITPB ONs or IHTPB ONs (IR780 concentration: 2.7 μg/mL), in the presence or absence of HA segments (10 mg/mL), at 37°C for 4 h. Cells treated with free IR780 served as the control group. After fixation with 4% formaldehyde and nuclear staining with Hoechst 33342, the cells were imaged using a confocal laser scanning microscope (CLSM; Olympus FluoView FV3000, Japan) with excitation wavelengths of 405 nm for Hoechst and 640 nm for IR780. Cellular internalization of IHTPB ONs was further quantified by flow cytometry (FACSCalibur, BD Bioscience). Following incubation with IHTPB ONs (IR780 concentration: 2.7 μg/mL), with or without HA segments, at 37°C for 4 h, B16F10 cells (2×10^5 cells/well) were analyzed for intracellular IR780 fluorescence.

The intracellular GSH levels of B16F10 cells subjected to different treatments were quantified using a DTNB assay. B16F10 cells (2×10^5 cells/well) were seeded in 6-well plates and incubated with free IR780, ITPB ONs, or IHTPB ONs (IR780 concentration: 2.7 μg/mL) for 4 h. The cells were then washed twice with PBS and detached using trypsin-EDTA. After centrifugation at 1500 rpm for 5 min, the collected cell pellets were either exposed to 808 nm NIR laser irradiation (1.0 W/cm^2) for 1 min or kept in the dark. Subsequently, the cells were lysed in RIPA buffer and frozen overnight. After thawing, the lysates were centrifuged at 12 000 rpm for 10 min, and the resulting supernatants were reacted with DTNB. The absorbance was measured at 405 nm using a microplate reader. For comparison, intracellular GSH levels in B16F10 cells treated with HTPB ONs (22.2 μg/mL), with or without NIR laser irradiation, were also determined.

The intracellular O_2 level of B16F10 cells receiving different treatments was determined with the $[Ru(dpp)_3]Cl_2$ assay. B16F10 cells (2×10^5 cells/well) seeded on round glass coverslips in 6-well plates were incubated with IR780 molecules, ITPB ONs, or IHTPB ONs (IR780 concentration: 2.7 μg/mL) for 4 h and either exposed to an 808 nm NIR laser (1.0 W/cm^2) for 5 min or left unirradiated. After being fixed with 4% formaldehyde and stained with $[Ru(dpp)_3]Cl_2$ (10 μM), the cells were imaged using fluorescence microscopy (ZEISS Axio Imager M2) at an excitation wavelength of 488 nm. For comparison, the intracellular O_2 level of B16F10 cells incubated with HTPB ONs (22.2 μg/mL) in the presence or absence of NIR laser irradiation was also assessed.

The intracellular ROS generation in B16F10 cells under different treatments was evaluated using a DCFH-DA assay. B16F10 cells (2.0×10^5 cells/well) were seeded on round glass coverslips in 6-well plates and cultured for 24 h. The cells were then incubated with free IR780, ITPB ONs, or IHTPB ONs (IR780 concentration: 2.7 μg/mL) for 4 h, followed by either exposure to 808 nm NIR laser irradiation (1.0 W/cm^2) for 5 min or no irradiation. After incubation with DCFH-DA (5 μM), intracellular DCF fluorescence was observed using a fluorescence microscope (ZEISS Axio Imager M2) with an excitation wavelength of 485 nm. For comparison, intracellular ROS levels in B16F10 cells treated with HTPB ONs (22.2 μg/mL), with or without NIR laser irradiation, were also assessed.

2.12 | Intracellular Mitochondrial Damage and LPO

To assess the impact of different formulations on mitochondria, a JC-1 staining assay was used to monitor changes in mitochondrial transmembrane potential. B16F10 cells (2.0×10^5 cells/well) cultured on round glass coverslips were incubated with free IR780, ITPB ONs, or IHTPB ONs (IR780 concentration: 2.7 μg/mL) for 4 h, followed by either 808 nm NIR laser irradiation (1.0 W/cm^2) for 5 min or no irradiation. The cells were then stained with JC-1 (2 μM) and imaged using a fluorescence microscope (ZEISS Axio Imager M2), with excitation wavelengths of 485 and 535 nm to detect JC-1 monomers and aggregates, respectively. For comparison, JC-1 staining was also performed on B16F10 cells treated with HTPB ONs (22.2 μg/mL) under laser irradiation.

Intracellular LPO was assessed using the BODIPY581/591 C11 assay. B16F10 cells (1.0×10^5 cells/well) cultured on round glass coverslips in 6-well plates were incubated with free IR780, ITPB

ONs, or IHTPB ONs (IR780 concentration: 2.7 μg/mL) for 4 h, followed by either 808 nm NIR laser irradiation (1.0 W/cm^2) for 5 min or no irradiation. The cells were then stained with 2 μM BODIPY581/591 C11 and imaged using a fluorescence microscope (ZEISS Axio Imager M2) with an excitation wavelength of 500 nm. For comparison, B16F10 cells treated with HTPB ONs (22.2 μg/mL) under laser irradiation were also examined.

2.13 | In Vitro Anticancer Potency

B16F10 cells (2.0×10^5 cells/well) seeded in 6-well plates were incubated with free IR780, ITPB ONs, or IHTPB ONs at varying IR780 concentrations for 4 h at 37°C. The cells were then washed with PBS, detached using trypsin-EDTA, and centrifuged at 1500 rpm. The resulting cell pellets were either exposed to 808 nm NIR laser irradiation (1.0 W/cm^2) for 1 min or left unirradiated. After reseeding in 12-well plates, the cells were incubated for an additional 24 h. Cell viability was determined using the MTT assay according to the manufacturer's instructions. The cytotoxicity of the same formulations was also evaluated on CT26 cells following the same procedure. For comparison, the effects of HTPB ONs, with and without laser irradiation, on both B16F10 and CT26 cells were assessed in a similar manner.

The anticancer activity of the different formulations on B16F10 cells was further evaluated using calcein-AM and PI staining to distinguish live and dead cells. B16F10 cells (2×10^5 cells/well) seeded in 12-well plates were incubated with free IR780, ITPB ONs, or IHTPB ONs (IR780 concentration: 2.7 μg/mL) for 4 h, followed by either 808 nm NIR laser irradiation (1.0 W/cm^2) for 1 min or no irradiation. The cells were then stained with calcein-AM (2 μM) and PI (4.5 μM) and imaged using a NIB-100F inverted fluorescence microscope.

2.14 | In Vitro Hemolysis Assay

The hemocompatibility of IHTPB ONs was assessed using a hemolysis assay. Whole blood was collected from male C57BL/6J mice, and red blood cells (RBCs) were isolated by centrifugation. A 2% (v/v) RBC suspension was incubated with IHTPB ONs at various concentrations for 1 h. Following incubation, the samples were centrifuged, and the absorbance of the supernatant was measured at 570 nm to determine the hemolysis rate. RBCs incubated with deionized water and 0.9% saline served as the positive and negative controls, respectively.

2.15 | Animals and Tumor Model

Male C57BL/6J mice (5–6 weeks old) were obtained from the National Laboratory Animal Center (Taiwan). All animal experiments (IACUC Approval No: 112040) were conducted in accordance with the guidelines approved by the Administrative Committee on Animal Research at Chung Shan Medical University (Taiwan). To establish the tumor model, 1×10^6 B16F10 cells were injected subcutaneously into the right thigh of each mouse. Tumor volume (V) was estimated using the formula $V = L \times W^2/2$, where L represents the longest dimension and W the widest measurement of the tumor.

2.16 | In Vivo Biodistribution

When tumor volumes reached 80–110 mm^3, the mice were randomly assigned to three groups ($n = 3$ each): (1) free IR780, (2) ITPB ONs, and (3) IHTPB ONs. Each mouse received an intravenous tail-vein injection of 100 μL of the respective solution, corresponding to an IR780 dose of 1.0 mg/kg. In vivo IR780 fluorescence was monitored at 1, 3, 6, and 24 h post-injection using an IVIS imaging system (IVIS Lumina II, USA). At 24 h post-injection, the mice were euthanized with CO_2, and the major organs and tumors were excised and imaged using the IVIS system.

2.17 | In Vivo Antitumor Effect

Once the B16F10 tumors in mice reached 80–110 mm^3, the animals were randomly assigned to five groups ($n = 4$ per group): (1) control, (2) IR780 + laser, (3) IHTPB ONs, (4) ITPB ONs + laser, and (5) IHTPB ONs + laser. On days 0 and 2, mice received tail-vein injections of 100 μL of the corresponding formulations (IR780 dose: 1.0 mg/kg). At 24 h post-injection, tumor sites were irradiated with an 808 nm laser (0.5 W/cm^2) for 5 min, and tumor temperatures were monitored using an infrared thermal imaging camera. Tumor volumes and body weights were recorded throughout the study. After treatment, mice were euthanized by CO_2 overdose, and tumors along with major organs (heart, liver, spleen, lung, and kidney) were collected. Tumors were weighed and photographed. Organs were sectioned into 4 μm-thick slices for hematoxylin and eosin (H&E) staining, while tumor sections were stained with H&E, anti-Ki67, anti-GPX4, and anti-HIF-1α antibodies. Images were captured using an Olympus IX70 inverted microscope (Japan).

2.18 | In Vivo Safety

To assess the blood biochemistry, the quantities of alanine aminotransferase (ALT), aspartate transaminase (AST), and blood urea nitrogen (BUN) as well as creatinine (CRE) in the serum of B16F10 tumor-bearing mice receiving IHTPB ONs (IR780 dose: 1.0 mg/kg) and laser irradiation were tested using an automatic blood biochemical analyzer (Hitachi 7600).

2.19 | Statistical Analysis

Data are expressed as mean ± SD. Differences between groups were analyzed using one-way or two-way ANOVA. Significance is indicated as follows: ns, $p > 0.05$; *$p < 0.05$; **$p < 0.01$; ***$p < 0.001$; ****$p < 0.0001$.

3 | Results and Discussions

3.1 | Preparation and Characterization of IHTPB ONs

The fabrication procedure of the IHTPB ONs is illustrated in Scheme 1a. First, PB ONs were synthesized by mixing $K_3[Fe(CN)_6]$, PVP, and HCl. Afterward, through the coordination

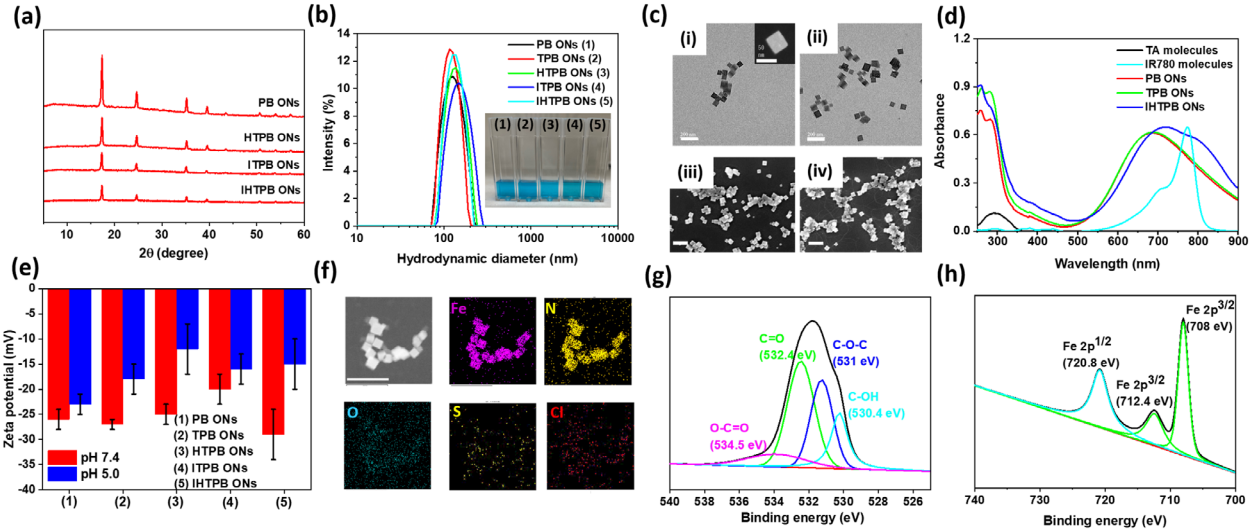

FIGURE 1 | (a) XRD patterns of various PB-based ONs. (b) Particle size distribution profiles of various PB-based ONs in deionized water. Inset: photos of various PB-based ON solutions. (c) TEM images of (i) PB ONs and (ii) TPB ONs and SEM images of (iii) PB ONs, and (iv) TPB ONs. Scale bar: 200 nm; scale bar of inset: 50 nm. (d) UV–Vis spectra of TA molecules, IR780 molecules, PB ONs, TPB ONs, and IHTPB ONs in pH 7.4 aqueous solutions. (e) Zeta potentials of different PB-based ONs dispersed in aqueous solutions at pH 7.4 and 5.0 ($n = 3$). (f) Elemental mapping of IHTPB ONs. Scale bars: 250 nm. (g and h) XPS spectra of IHTPB ONs showing O 1s and Fe 2p signals, respectively.

TABLE 1 | Particle size and IR780-loading characterization of various PB-based ONs.

Sample	D_h (nm)	PDI	Loading efficiency (%)	Loading content (wt %)
PB ONs	113 ± 10	0.16 ± 0.02	—	—
TPB ONs	123 ± 2	0.12 ± 0.05	—	—
HTPB ONs	134 ± 5	0.15 ± 0.03	—	—
ITPB ONs	166 ± 10	0.14 ± 0.03	85 ± 3	12.5 ± 1.1
IHTPB ONs	155 ± 9	0.15 ± 0.05	91 ± 1	11.5 ± 1

between TA molecules and Fe^{2+}/Fe^{3+} ions, TA molecules were attached onto the surface of PB ONs. The positively charged IR780 molecules were incorporated into TA-coated PB ONs upon multiple interactions between IR780 and TA. Finally, the surfaces of IHTPB ONs were modified with HA layers via Michael addition of HA-SH and TA. As presented in the XRD pattern of the as-synthesized PB ONs (Figure 1a), the diffraction peaks at 17.5°, 24.7°, 35.5°, and 39.7° were observed, being comparable to those reported previously [47]. Moreover, the aqueous solution of PB ONs displays a characteristic deep blue appearance (Figure 1b). These results confirm the successful synthesis of PB ONs. The PB ONs exhibited an average hydrodynamic diameter of approximately 113 nm with a monodisperse size distribution (PDI = 0.16) in deionized water (Table 1 and Figure 1b). Moreover, the TEM and SEM images showed a uniform cubic shape of PB ONs with ca 45 nm average size (Figure 1c). A visible feature absorption of PB ONs at 690 nm was attained (Figure 1d), being similar to that reported elsewhere [48, 49]. After being covered with TA molecules, the PB ONs showed a slightly increased particle size from 113 nm to 123 nm (Table 1 and Figure 1b). Additionally, at the same PB concentration, the TPB ONs showed a higher absorption at 300 nm compared to the PB ONs (Figure 1d). As revealed in the FT-IR spectra of TPB ONs (Figure S2), in addition to the absorption band of C≡N stretching vibration at 2069 cm^{-1} from PB ONs, two feature absorption bands of C—O—C and C═C stretching vibration at 1045 and 1616 cm^{-1}, respectively, from TA molecules were observed. These findings suggest the successful coating of TA molecules on the surfaces of PB ONs. The TA adsorption content of TPB ONs was determined to be ca 14 wt%. The XRD patterns and TEM/SEM images revealed that the TPB ONs retained a well-defined crystal structure and a uniformly dispersed cubic morphology, similar to that of the PB ONs (Figure 1a,c). To equip the TPB ONs with tumor-targeting capabilities, the HA-SH segments were decorated on the surfaces of TPB ONs. As presented in Figures 1a and S3, the HTPB ONs retained a PB-like crystal structure and cubic shape, suggesting that the covalent modification of HA segments on the surfaces of TPB ONs could not impair the original conformation. Additionally, compared to TPB ONs, the HTPB ONs exhibited a slightly larger particle size due to the presence of an HA-rich surface layer (Table 1 and Figure 1b). Based on TGA profiles (Figure S4), the HTPB ONs consist of 86% TPB ONs and 14 wt% HA.

Taking advantage of the negatively charged phenol group-rich surfaces of TPB ONs, the cationic and lipophilic IR780 molecules were attached onto their surfaces upon π–π stacking, electrostatic attraction, and hydrogen bonding. Notably, the ionic pairing of

phenolic hydroxyl groups from TPB ONs with the quaternary ammonium group of IR780 led to a conversion in zeta potential from −27 mV (for TPB ONs) to −20 mV (for ITPB ONs) (Figure 1e). Next, through the Michael addition between HA-SH segments and TA-rich surfaces of ITPB ONs, the IHTPB ONs were attained. Notably, in addition to the signals of Fe and N elements from PB ONs (Figure S5), the signals of O elements from TA and HA-SH, S elements from HA-SH, and Cl elements from IR780 were observed in the EDS elemental maps of IHTPB ONs (Figure 1f). Furthermore, the zeta potential results show that the surfaces of IHTPB ONs have more negative charges than those of ITPB ONs (Figure 1e). As presented in the O 1s XPS spectrum of IHTPB ONs, two binding energy peaks at 532.4 and 534.5 eV corresponding to C═O and O─C═O from HA-SH segments were observed (Figure 1g). These findings demonstrate the successful conjugation of carboxylic acid group-rich HA-SH segments with the TA-rich surfaces of ITPB ONs. As shown in Figure 1a,f, the IHTPB ONs exhibited a PB-like crystal structure and cubic morphology. In addition, the binding energy peaks at 708 and 720.8 eV, assigned to Fe^{2+}, and the peaks at 712.4 eV, ascribed to Fe^{3+}, were attained in the high-resolution Fe 2p spectrum of IHTPB ONs (Figure 1h). These results indicate that the IHTPB ONs maintained the intact PB architecture. Compared to free IR780, the IHTPB ONs showed an appreciable red shift in the IR780 absorption (Figure 1d), indicating the effective encapsulation of IR780 into HA/TA-constituted layers upon the π–π stacking, electrostatic interaction, and hydrogen bonding. As shown in Table 1, the IR780 loading efficiency of ITPB ONs and IHTPB ONs is 85% and 91%, respectively. Although both formulations had similar drug-loading capacities, the IHTPB ONs maintained a nearly constant particle size over 24 h when dispersed in 0.15 M PBS at pH 7.4 (Figure S6), whereas the ITPBs showed a significant increase in particle size within just 1 h under the same conditions. Notably, after dispersion in DMEM containing 10% FBS for 24 h, the IHTPB ONs maintained an almost unchanged particle size (Figure S7), indicating their excellent colloidal stability. These findings demonstrate that the hydrophilic HA layer plays a key role in promoting the colloidal stability of IHTPB ONs. In contrast, in the absence of HA decoration, ITPB ONs tended to undergo hydrophobic aggregation into larger particles under physiological salt conditions, owing to the exposure of lipophilic IR780 molecules on their surfaces. Interestingly, IHPB ONs exhibited a markedly increased size in pH 7.4 PBS, indicating their aggregation (Figure S6). This suggests that the absence of TA decoration on the PB ON surface results in insufficient HA-SH conjugation and unstable IR780 adsorption, thereby diminishing the colloidal stability of IHPB ONs. Based on the above results, surface modification of the PB ONs with both TA and HA-SH is crucial for improving the colloidal stability and dispersion of IHTPB ONs.

3.2 | Photothermal Effect and Stability of IHTPB ONs

Leveraging the intrinsic ability of PB ONs and IR780 to convert NIR light into heat, the photothermal performance of IHTPB ONs was evaluated by monitoring the temperature changes of their aqueous solutions under NIR laser irradiation using an infrared thermal imaging camera. At an equivalent IR780 concentration (9 μg/mL), the solutions of IHTPB ONs and ITPB ONs exhibited significantly higher temperature increases under NIR irradiation compared with the free IR780 solution (Figure 2a). In addition, PB ONs exhibited a notable temperature rise under laser irradiation. From the photothermal heating–cooling curves (Figure 2b), the photothermal conversion efficiency (η) of IHTPB ONs was calculated to be approximately 60%, slightly higher than that of PB ONs (50%) (Figure S8a). In contrast, free IR780 molecules displayed a low photothermal conversion efficiency of about 2.9% (Figure S8b), attributable to their absorption peak near 780 nm, which is substantially offset from the 808 nm NIR laser, as well as pronounced self-aggregation. Based on these findings, the incorporation of IR780 molecules into the HTPB ONs resulted in an additive effect on the photothermal conversion efficiency of the IHTPB ONs. This aligns with the results showing that IHTPB ONs exhibit a superior photothermal effect compared to PB ONs and free IR780 molecules at prescribed concentrations of PB and IR780 (Figure 2a). As expected, the temperature increase of the IHTPB ON solution under laser irradiation was enhanced either by increasing the concentration of IHTPB ONs or by elevating the laser power density (Figure S9). Notably, both IHTPB ONs and ITPB ONs retained nearly intact photothermal performance after undergoing three on/off cycles of NIR laser irradiation (Figure 2c). In contrast, the free IR780 molecules exhibited a significantly reduced photothermal effect. As presented in Figures 2d and S10, after three on/off cycles of NIR laser irradiation, compared to a visible decrease in the absorption of free IR780 molecules due to severe photobleaching, only a minor decline in the absorption of IHTPB ONs was observed. These results indicate that IHTPB ONs and ITPB ONs not only demonstrate excellent photothermal conversion performance but also reduce photobleaching of IR780 molecules by the electron transition between Fe^{2+} and Fe^{3+} from PB, thereby maintaining a stable photothermal effect. This makes them promising candidates for enhancing the efficacy of phototherapy-based anticancer treatments.

3.3 | GSH-Depleting Performance and In Vitro IR780 Liberation of IHTPB ONs

Taking advantage of the reversible redox property of Fe^{2+} and Fe^{3+}, PB has been demonstrated to consume GSH [48, 50]. Moreover, some studies report that nucleophilic reactions, including quinone–phenol dismutation, Schiff base formation, and Michael addition, take place between *o*-quinone and substrates containing catechol, amine, or thiol groups [51]. Owing to the abundant quinone groups in TA and the amine and thiol residues in GSH, we hypothesized that TA could conjugate with GSH through Schiff base formation and Michael addition, thereby inducing GSH depletion. Based on these viewpoints, the GSH-depleting capability of IHTPB ONs was evaluated by the DTNB assay. As shown in Figure 2e, compared to the control group (GSH alone + DTNB), the absorption of DTNB in the GSH solution pretreated with TA or PB ONs at 37°C for 6 h appreciably decreased. In addition, TA molecules and PB ONs induced a cumulative GSH depletion of approximately 31% (Figure S11). This suggests that TA depletes GSH via nucleophilic reactions, whereas the PB ONs consume GSH through the Fe^{2+}/Fe^{3+} redox cycle. Notably, a remarkable decline in the absorption of DTNB was observed in the GSH solution pretreated with IHTPB ONs at 37°C for 6 h. The IHTPB ONs and HTPB ONs realized cumulative

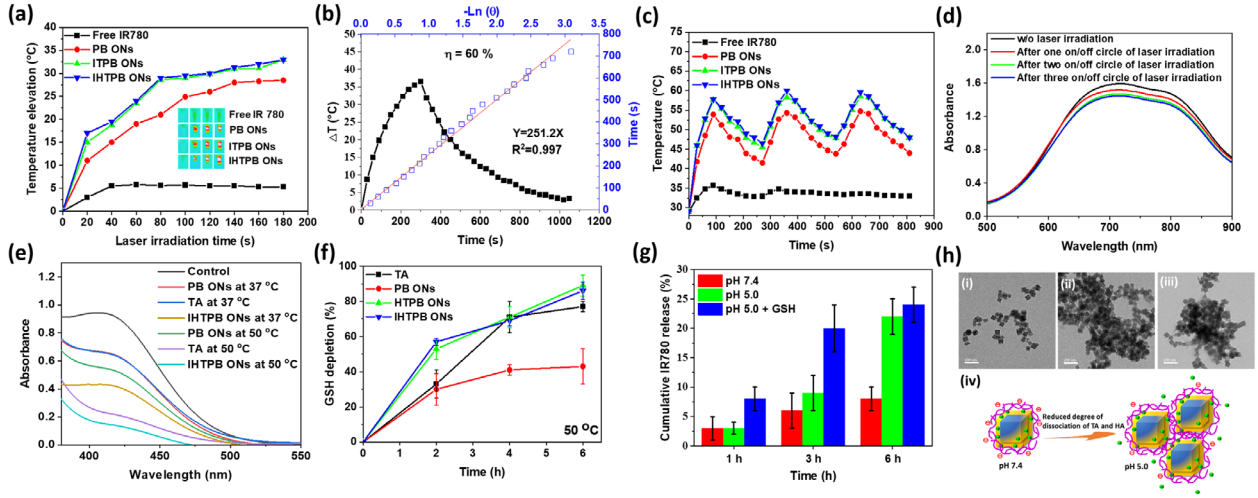

FIGURE 2 | (a) Temperature elevation curves of free IR780, PB ONs, ITPB ONs, and IHTPB ONs in deionized water under 808 nm laser irradiation (1.0 W/cm^2). (b) Temperature changes of IHTPB ONs (IR780 concentration: 9 μg/mL) during a single on/off cycle of 808 nm laser irradiation (1.0 W/cm^2), with corresponding plots of cooling time versus the negative logarithm of the temperature driving force. (c) Temperature profiles of PB ONs (50 μg/mL), free IR780, ITPB ONs, and IHTPB ONs (IR780 concentration: 9 μg/mL) over three consecutive 808 nm NIR laser on/off cycles (1.0 W/cm^2). (d) UV–Vis spectra of IHTPB ONs in deionized water after repeated NIR laser on/off cycles. (e) Absorption spectra of DTNB reacted with GSH pretreated with TA molecules, PB ONs, and IHTPB ONs, respectively, at 37°C and 50°C for 6 h. (f) Cumulative GSH depletion of TA molecules, PB ONs, HTPB ONs, and IHTPB ONs at 50°C over 6 h ($n = 3$). (g) Cumulative IR780 release profiles of IHTPB ONs under different conditions ($n = 3$). (h) TEM images of IHTPB ONs at (i) pH 7.4, (ii) pH 5.0, and (iii) pH 5.0 with GSH. Scale bars: 200 nm. Inset: (iv) Scheme of acidity-triggered aggregation of IHTPB ONs.

GSH depletion of about 56% and 53%, respectively, exceeding that of TA molecules and PB ONs (Figure S11). These results suggest that the integration of TA and PB ONs endowed IHTPB ONs and HTPB ONs with a markedly enhanced GSH-depleting capacity compared to either TA molecules or PB ONs alone. As the reaction temperature was elevated from 37°C to 50°C, a pronounced decrease in DTNB absorption was observed in GSH solutions treated with TA molecules, HTPB ONs, or IHTPB ONs for 6 h, compared to those treated with PB ONs (Figure 2e). In addition, for TA molecules, HTPB ONs, and IHTPB ONs, the cumulative GSH depletion of around 77%, 89%, and 86% was attained at 50°C over 6 h (Figure 2f). The results indicate that TA molecules and IHTPB ONs achieve thermally enhanced GSH depletion through the accelerated TA-mediated Schiff base reaction and Michael addition at elevated temperatures. In view of the aforementioned PB/IR780-mediated photothermal effect, it was expected that the NIR-triggered hyperthermia of IHTPB ONs would efficiently promote GSH depletion, thereby reducing the scavenging of singlet oxygen by GSH and enhancing the anticancer efficacy of ROS-based therapy.

Given the short half-life and limited diffusion distance of $^1O_2$, efficient intracellular delivery of IR780 is crucial for enhancing ROS-mediated anticancer efficacy. Considering the weakly acidic (pH 4.5–6.0) and GSH-rich (2–10 mM) intracellular environment of cancer cells, the in vitro release of IR780 from IHTPB ONs was investigated under varying pH conditions and in the presence of GSH. As shown in Figure 2g, the cumulative release of IR780 from IHTPB ONs at pH 7.4 (simulating normal physiological conditions) over 6 h was 7.6%, which was markedly lower than the 21.5% release observed at pH 5.0 (mimicking intracellular acidic organelles). Furthermore, as the solution pH was adjusted from 7.4 to 5.0, the IHTPB ONs showed a significant conversion in zeta potential from −29 mV to −15 mV (Figure 2a). Similar acidity-triggered zeta potential change was also observed in TPB ONs and HTPB ONs. These results indicate that under acidic conditions, the dissociation of phenolic hydroxyl groups and carboxylic acid groups in the TA and HA layers is significantly reduced, resulting in a decrease in surface negative charge. This reduction likely weakens the electrostatic interactions between IR780 and the TA/HA layers, thereby facilitating the release of IR780 from IHTPB ONs. Notably, in the presence of 10 mM GSH, the release of IR780 from IHTPB ONs at pH 5.0 was profoundly accelerated. Given the nucleophilic reactions between TA and GSH, it was hypothesized that conjugation of TA with hydrophilic GSH molecules could further weaken the π–π stacking interactions between TA and IR780, thereby facilitating the release of IR780 from IHTPB ONs. Based on the above results, the acidity/GSH-enhanced IR780 release of IHTPBs ONs was anticipated to realize the intracellular IR780 delivery for maximizing the $^1O_2$-driven anticancer effect. On the other hand, the IHTPB ONs exhibited a visibly enlarged particle size at pH 5.0 with or without GSH (Figure S12). Also, a substantial aggregation of IHTPB ONs was found in their TEM images (Figure 2h). These results indicate that the acidity-elicited decline in the degree of dissociation of carboxylic acid residues of HA layers could largely decrease the electrostatic repulsion between IHTPB ONs, thus provoking interparticle aggregation.

3.4 | O_2- and $^1O_2$-Producing Performance of IHTPB ONs

PB nanoparticles have been demonstrated to exert catalase-like activity capable of converting H_2O_2 at tumor sites into O_2, thus alleviating tumor hypoxia [32–34]. Therefore, the O_2-generating capability of PB ONs and IHTPB ONs in H_2O_2-containing solution was evaluated using a portable dissolved

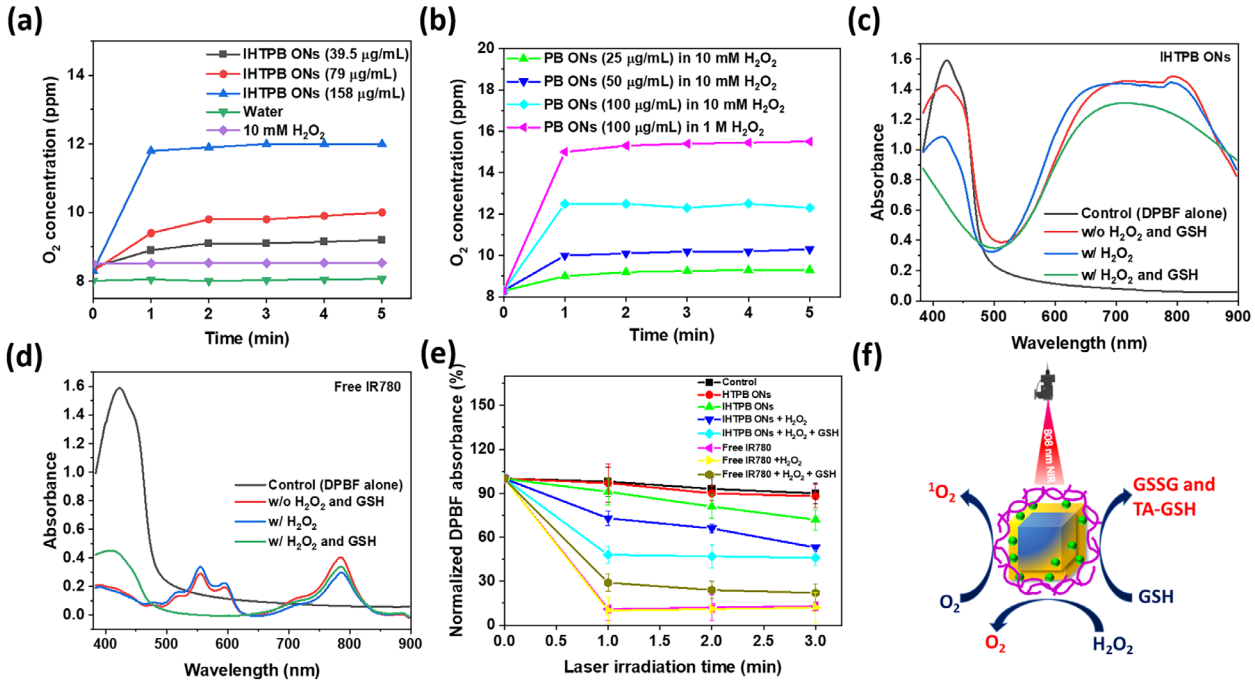

FIGURE 3 | O_2 generation curves after mixing different concentrations of (a) IHTPB ONs and (b) PB ONs with H_2O_2 (10 mM or 1 M). Absorption spectra of DPBF in (c) IHTPB ON solutions or (d) free IR780 solutions, with or without H_2O_2 and GSH, after 1 min of laser irradiation. (e) Normalized absorbance of DPBF molecules treated with various formulations and laser irradiation for different times ($n = 3$). (f) Schematic illustration of the self-depleting GSH, self-supplying O_2, and NIR-triggered $^1O_2$ production by IHTPB ONs.

oxygen meter. Different from the nearly unchanged oxygen level of the pure water and 10.0 mM H_2O_2 solution, the O_2 level of the IHTPB ONs in 10.0 mM H_2O_2 solutions rapidly rises with increasing concentration of IHTPB ONs (Figure 3a). A similar concentration-dependent O_2 production was also attained in PB ONs (Figure 3b). Furthermore, as the H_2O_2 concentration was increased from 10 mM to 1 M, the PB ONs produced more oxygen. These results illustrate the sound catalase-like activity of IHTPB ONs.

Thereafter, the photodynamic effects of IHTPB ONs in the solution were assessed. In this work, $^1O_2$ production in the solution was investigated using DPBF as the $^1O_2$ indicator. When the DPBF reacted with $^1O_2$, the absorption of DPBF at 410 nm was decreased. As shown in Figure S13, no significant variation in the absorption of DPBF in the HTPB group receiving 808 nm laser irradiation was observed. In contrast, with 1-min NIR laser irradiation, the absorption of DPBF in aqueous solutions containing free IR780 molecules or IHTPB ONs was reduced (Figure 3c,d), indicating $^1O_2$ production based on the IR780-mediated photodynamic effect. Moreover, with prolonged laser irradiation from 1 min to 3 min, a gradual decrease in the normalized DPBF absorbance was observed in the IHTPB ON group, signifying increased $^1O_2$ generation (Figure 3e). Under the 1-min laser irradiation duration, the DPBF absorption in the free IR780 group decreased much more significantly than in the IHTPB ON group (Figure 3c,d), suggesting that free IR780 molecules could generate $^1O_2$ more efficiently due to their ample interaction with the surrounding O_2.

Furthermore, upon the addition of 10 mM H_2O_2 and subsequent 1-min laser irradiation, the DPBF absorbance in the IHTPB ON group further decreased, whereas that in the free IR780 group remained nearly unchanged. Notably, in the presence of H_2O_2, the normalized DPBF absorbance of the IHTPB ON group further decreased with prolonged laser irradiation, whereas that of the free IR780 group showed no appreciable change (Figure 3e). These results verify that the IHTPB ONs can convert H_2O_2 into O_2 through PB-mediated catalase-like activity, thereby promoting IR780-based photodynamic effect to produce more $^1O_2$. In contrast, due to the lack of catalase-like activity, the $^1O_2$-producing performance of IR780 molecules was not enhanced in the presence of H_2O_2. Importantly, in the presence of both H_2O_2 and GSH, the normalized DPBF absorbance of the IHTPB ON group was remarkably decreased to approach that of the free IR780 group during laser irradiation. This could be attributed to the following reasons. First, the IR780 release from IHTPB ONs was accelerated under the GSH-containing condition, thus facilitating the contact of IR780 with surrounding O_2 to augment $^1O_2$ production. Furthermore, the PB/TA-mediated GSH depletion could effectively reduce the scavenging of $^1O_2$ by residual GSH. By contrast, the $^1O_2$ generated from free IR780 molecules was partly consumed by GSH. Based on the above findings, it is concluded that the IHTPB ONs can efficiently deplete GSH and degrade H_2O_2 to O_2, thereby maximizing $^1O_2$ production upon IR780-elicited photodynamic activity (Figure 3f).

3.5 | In Vitro Cellular Uptake, GSH Depletion, O_2, and $^1O_2$ Production

B16F10 cells are among the most frequently used murine melanoma models with high CD44 expression and are commonly utilized for in vivo tumor and metastasis research. To evaluate

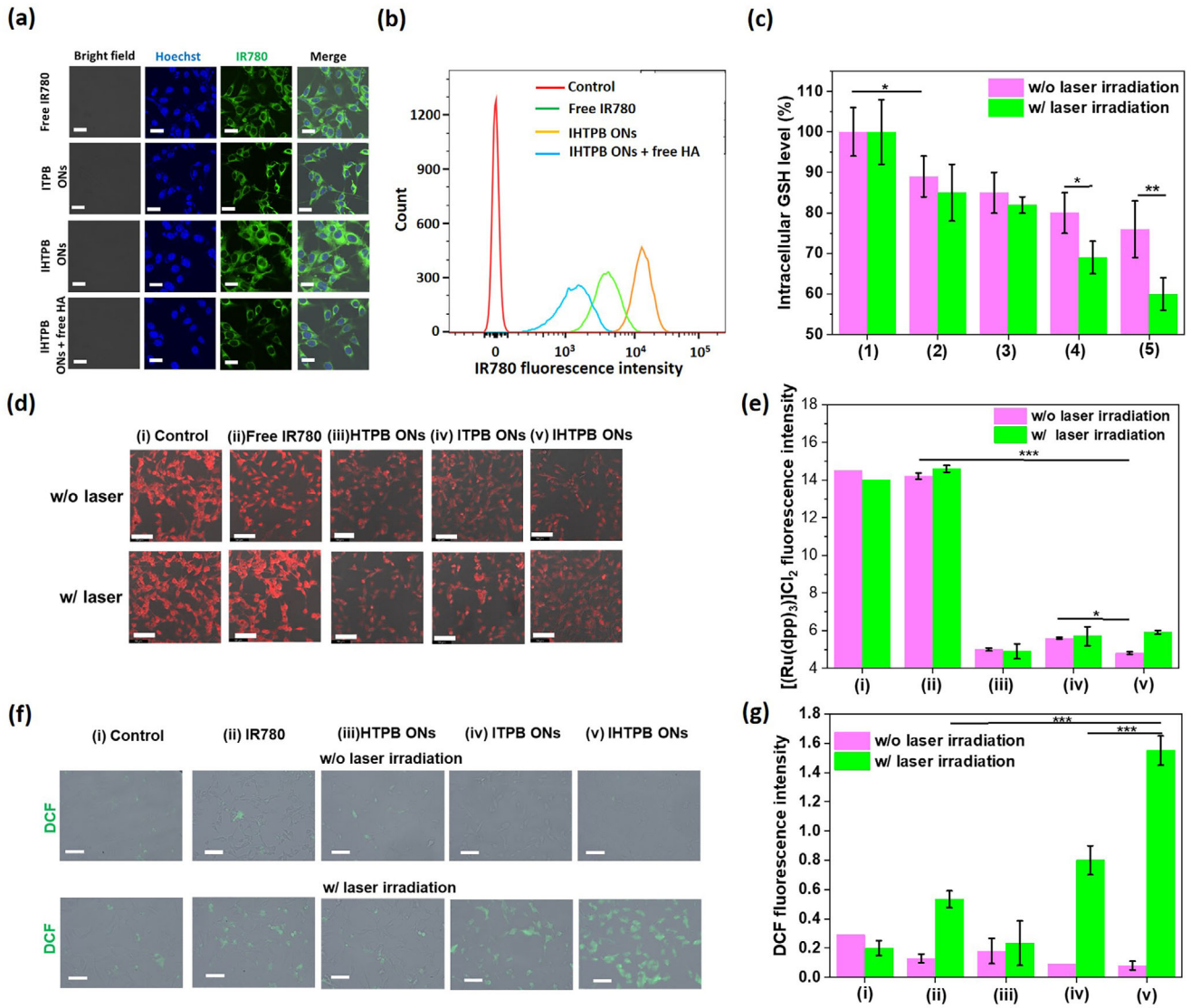

FIGURE 4 | (a) CLSM images of B16F10 cells incubated with various IR780-containing formulations at 37°C for 4 h. Scale bar: 20 μm. (b) Flow cytometric analysis of B16F10 cells treated with IR780 molecules or IHTPB ONs, with or without free HA segments, at 37°C for 4 h. (c) Intracellular GSH level of B16F10 cells treated with (1) PBS (control), (2) PB ONs, (3) TA molecules, (4) HTPB ONs, or (5) IHTPB ONs and with or without laser irradiation ($n = 3$). (d) $Ru(dpp)_3Cl_2$ staining (scale bar: 50 μm) and (e) corresponding fluorescence quantification of B16F10 cells receiving various treatments ($n = 3$). (f) DCF fluorescence images (scale bar: 50 μm) and (g) corresponding fluorescence quantification of B16F10 cells subjected to various treatments ($n = 3$).

the HA-mediated CD44-targeting capability of IHTPB ONs, their cellular uptake by CD44-overexpressing B16F10 cells was examined using CLSM and flow cytometry. As shown in the CLSM images (Figure 4a), after 4 h of incubation, B16F10 cells treated with IHTPB ONs exhibited markedly stronger IR780 fluorescence than those co-treated with IHTPB ONs and free HA segments. Consistent results were obtained from flow cytometry analysis (Figure 4b). Moreover, after 4 h of incubation, B16F10 cells treated with IHTPB ONs exhibited stronger intracellular IR780 fluorescence than those exposed to ITPB ONs (without HA surface decoration). Compared with the ITPB ONs, the IHTPB ONs exhibited markedly enhanced cellular uptake, indicating that HA surface modification facilitates nanoparticle internalization. Moreover, the uptake was partially reduced after pretreatment with excess free HA, further suggesting the involvement of CD44 receptor-mediated endocytosis. Nevertheless, because receptor-specific genetic or pharmacological validation was not performed, these findings should be regarded as supportive rather than definitive evidence for CD44-mediated uptake.

Next, the DTNB assay was employed to assess the intracellular GSH-consuming capacity of IHTPB ONs. Without NIR laser irradiation, B16F10 cells treated with PB ONs or TA molecules showed moderately reduced intracellular GSH levels compared with the control group (Figure 4c), indicating that both PB ONs and TA molecules were able to partially deplete GSH, consistent with the results shown in Figures 2e and S11. Furthermore, B16F10 cells treated with IHTPB ONs or HTPB ONs exhibited a more pronounced decrease in GSH levels, attributable to the combined GSH-depleting effects of PB and TA. Upon NIR laser irradiation, while PB ONs or TA molecules alone induced no obvious reduction in intracellular GSH, cells treated with IHTPB ONs or HTPB ONs showed a significant depletion of GSH. These results indicate that the PB- and IR780-induced photothermal

effect markedly enhances GSH consumption by accelerating the TA-mediated Michael addition reaction. This observation is consistent with the results presented in Figure 2f. Notably, owing to the oxidation of GSH by $^1O_2$ generated through the IR780-mediated photodynamic effect, IHTPB ONs demonstrated a superior GSH-depleting capability compared with HTPB ONs.

To verify the feasibility of IHTPB ONs in alleviating hypoxia, we further evaluate the catalase-like activity of IHTPB ONs in B16F10 cells. Intracellular O_2 variations were monitored by fluorescence imaging using $Ru(dpp)_3Cl_2$ as an oxygen probe, whose fluorescence is quenched in the presence of O_2 [52]. As presented in Figure 4d,e, without NIR laser irradiation, the $Ru(dpp)_3Cl_2$ fluorescence signals of B16F10 cells treated with various PB-containing ONs were visibly lower than those of cells without any treatment (control group) or incubated with free IR780 molecules. This demonstrates that the PB-containing ONs can increase intracellular O_2 content through PB-mediated catalase-like activity, thus alleviating intracellular hypoxia. With NIR laser irradiation, B16F10 cells incubated with various PB-containing ONs maintained nearly unchanged $Ru(dpp)_3Cl_2$ fluorescence intensity, indicating that the ample O_2 generated through the catalase-like activity of PB could counterbalance the O_2 consumption caused by the IR780-mediated photodynamic effect. Next, DCFH-DA was used as a ROS probe to investigate the capability of IHTPB ONs to convert O_2 into $^1O_2$. In the absence of NIR irradiation, B16F10 cells subjected to different treatments displayed only negligible DCF fluorescence, comparable to that of the control group, indicating minimal $^1O_2$ production (Figure 4f,g). Upon NIR laser irradiation, however, the IR780, ITPB ON, and IHTPB ON groups exhibited markedly enhanced intracellular DCF fluorescence relative to the control and HTPB ON groups, demonstrating effective intracellular ROS generation driven by the photodynamic activity of IR780. Furthermore, due to scavenging of $^1O_2$ by endogenous GSH and the lack of supplementary O_2 supply, free IR780 generated substantially less ROS in B16F10 cells than ITPB ONs and IHTPB ONs, as evidenced by the weaker DCF fluorescence signals. Notably, compared with ITPB ONs, IHTPB ONs were more efficiently internalized via HA-mediated CD44 targeting, thereby facilitating intracellular GSH depletion and O_2 generation, which collectively enhanced $^1O_2$ production.

3.6 | Intracellular Mitochondrial Dysfunction and LPO

An increasing number of studies have shown that $^1O_2$ induces mitochondrial damage by directly oxidizing intermembrane components, including the electron transport chain and lipids, ultimately resulting in mitochondrial dysfunction [53, 54]. In addition, early-stage apoptosis is typically associated with a loss of mitochondrial membrane potential. Accordingly, JC-1, a probe sensitive to changes in mitochondrial transmembrane potential, was employed to evaluate the effects of $^1O_2$ generated by IHTPB ONs on the mitochondria of B16F10 cells. In the absence of NIR laser irradiation, B16F10 cells treated with free IR780 or various PB-based ONs exhibited minimal green fluorescence (JC-1 monomers) and strong red fluorescence (JC-1 aggregates), comparable to the control group, indicating preserved mitochondrial integrity. Upon NIR irradiation, however, cells incubated with IHTPB ONs displayed a pronounced increase in green fluorescence accompanied by a reduction in red fluorescence compared with those treated with free IR780, HTPB ONs, or ITPB ONs (Figure 5a). In conjunction with the intracellular $^1O_2$ generation results (Figure 4f,g), these observations indicate that the abundant $^1O_2$ produced by endocytosed IHTPB ONs under laser irradiation effectively disrupts mitochondrial integrity. By comparison, free IR780 or ITPB ONs induce only partial mitochondrial damage as a result of limited $^1O_2$ production. Moreover, in the absence of $^1O_2$ generation, photoinduced hyperthermia alone from HTPB ONs is insufficient to cause mitochondrial damage.

Accumulation of intracellular $^1O_2$ has been demonstrated to initiate LPO, thereby inducing ferroptosis, an iron-dependent form of programmed cell death [55, 56]. Subsequently, BODIPY 581/591 was employed as an LPO-sensitive fluorescent probe to assess LPO levels in B16F10 cells subjected to various treatments. In the absence of laser irradiation, treated B16F10 cells exhibited negligible green fluorescence signals (Figure 5b,c), indicating low basal LPO levels. In contrast, upon NIR laser irradiation, B16F10 cells treated with IHTPB ONs showed the most intense green fluorescence, exceeding that observed in cells treated with free IR780, HTPB ONs, or ITPB ONs. These results clearly demonstrate that, through CD44-mediated targeting and GSH self-depletion, IHTPB ONs significantly enhanced intracellular $^1O_2$ generation under NIR irradiation, thereby markedly promoting LPO. In contrast, treatment with free IR780 or non-CD44-targeting ITPB ONs led to only a limited increase in intracellular LPO levels due to insufficient $^1O_2$ generation. Based on these results, it was anticipated that IHTPB ONs, upon efficient internalization by B16F10 cells and subsequent NIR laser irradiation, would exhibit superior anticancer efficacy by synergistically inducing $^1O_2$-mediated mitochondrial damage, LPO, and ferroptosis in combination with hyperthermia (Scheme 1b).

3.7 | In Vitro Anticancer Effect and Blood Compatibility

The anticancer efficacy of IHTPB ONs against B16F10 cells was evaluated using an MTT assay to determine cell viability. As a control, in the absence of laser irradiation, B16F10 cells treated with HTPB ONs at concentrations ranging from 2.8 μg/mL to 44.4 μg/mL maintained viability above 90% (Figure 6a), demonstrating the negligible cytotoxicity of HTPB ONs toward cancer cells. In addition, B16F10 cells treated with free IR780, ITPB ONs, or IHTPB ONs exhibited cell viabilities exceeding 75%, with the modest reduction likely arising from the inherent dark toxicity of IR780. Notably, under NIR laser irradiation, IR780-treated B16F10 cells exhibited a moderate decrease in viability from 94% to 62% as the IR780 concentration increased from 0.4 μg/mL to 5.3 μg/mL (Figure 6b). In contrast, B16F10 cells treated with ITPB ONs or IHTPB ONs showed a pronounced reduction in cell viability over the same IR780 concentration range (Figure 6c,d). To further confirm the occurrence of ferroptosis, the viability of B16F10 cells treated with IHTPB ONs in combination with ferrostatin-1 (a ferroptosis inhibitor) under laser irradiation was evaluated. As shown in Figure S14, upon laser irradiation, the cell viability of B16F10 cells gradually increased from approximately 6% to 30% with increasing ferrostatin-1 concentration up to 8 μg/mL.

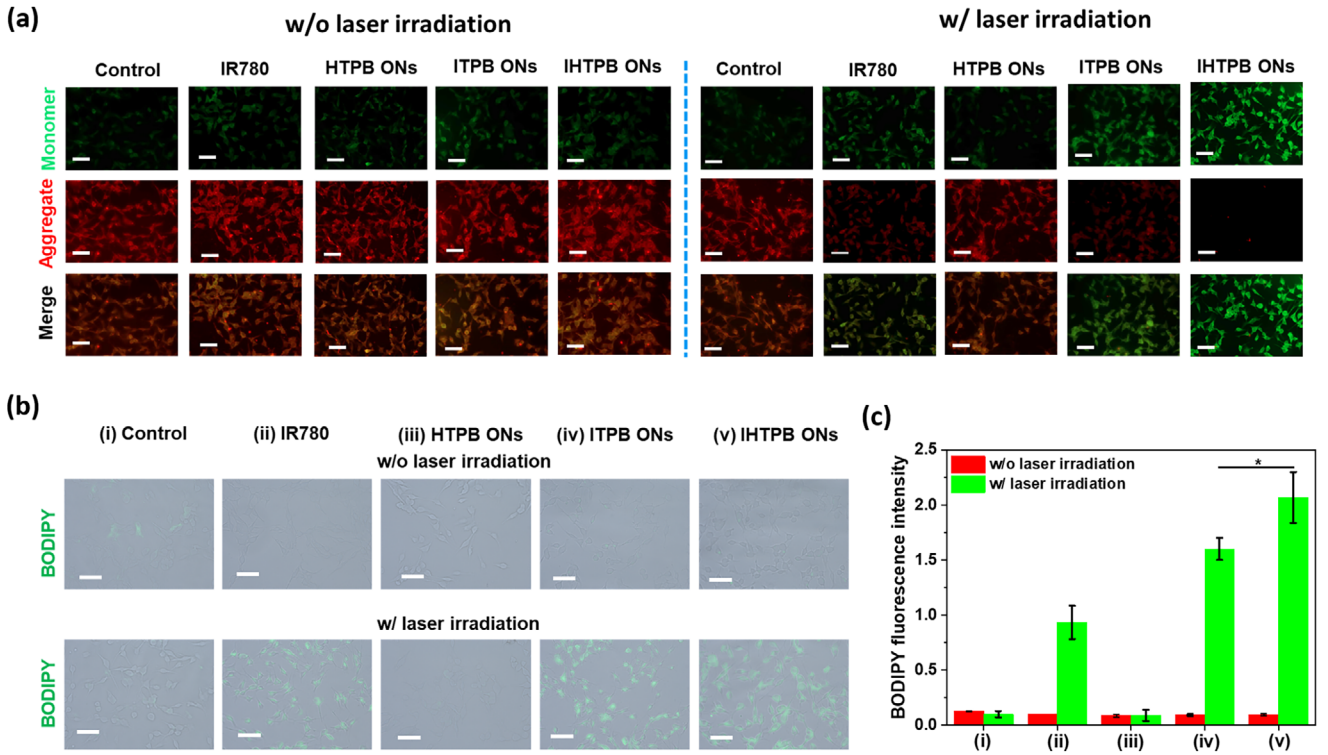

FIGURE 5 | (a) JC-1 staining images of B16F10 cells after different treatments. Scale bars: 50 μm. (b) BODIPY staining images and (c) corresponding fluorescence quantification of B16F10 cells under various treatments ($n = 3$). Scale bars: 50 μm.

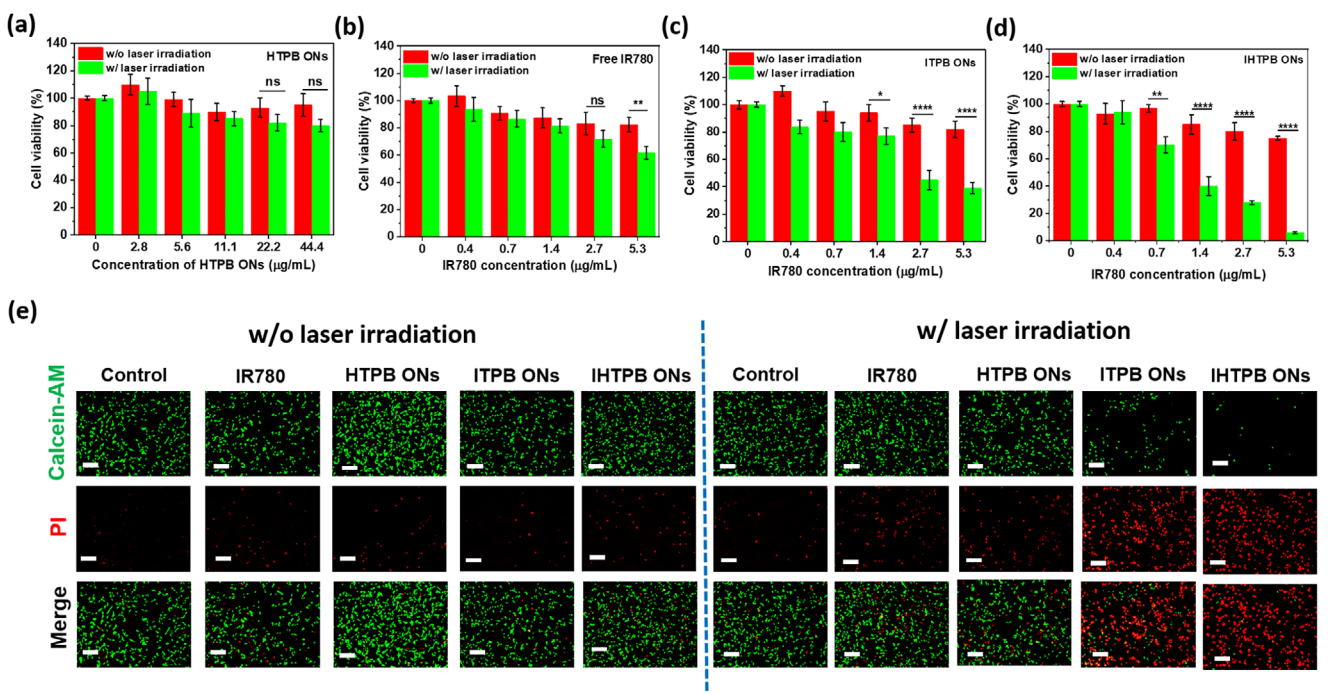

FIGURE 6 | Cell viability of B16F10 cells incubated with (a) HTPB ONs, (b) free IR780, (c) ITPB ONs, or (d) IHTPB ONs with or without laser irradiation ($n = 3$). (e) Calcein-AM/PI staining images of B16F10 cells subjected to various treatments. Scale bars: 200 μm.

These results further support that ferroptosis is involved in the IHTPB ONs-mediated cell death under laser irradiation. Clearly, compared with the limited anticancer efficacy of free IR780, intracellular delivery of IR780 via IHPB ONs or IHTPB ONs markedly enhanced NIR-induced $^1O_2$ generation and hyperthermia, owing to PB-based oxygen supply, PB/TA-mediated GSH depletion, and high photothermal conversion efficiency. These synergistic effects ultimately resulted in substantial cancer cell

death through mitochondrial damage, LPO, and ferroptosis. Furthermore, owing to enhanced cellular uptake mediated by HA-CD44 targeting, IHTPB ONs exhibited superior anticancer efficacy compared with ITPB ONs. Consistently, live/dead cell staining revealed that B16F10 cells treated with IHTPB ONs under laser irradiation displayed more pronounced PI staining than those subjected to other treatments (Figure 6e), further confirming the potent cytotoxicity of IHTPB ONs. In contrast, for HTPB ONs, the absence of sufficient $^1O_2$ generation rendered NIR-triggered hyperthermia alone minimally cytotoxic to B16F10 cells. Moreover, to further validate the enhanced anticancer efficacy of IHTPB ONs against CD44-overexpressing cancer cells, a CD44-overexpressing CT26 cell model was employed. Notably, owing to the synergistic effects of CD44-targeted delivery, NIR-triggered $^1O_2$ generation, and photothermal heating, IHTPB ONs exhibited significantly greater cytotoxicity toward CT26 cells than ITPB ONs lacking CD44-targeting ability (Figure S15). Collectively, these results underscore the ability of IHTPB ONs to effectively suppress the proliferation of CD44-overexpressing cancer cells under NIR-triggered phototherapy.

The blood compatibility of IHTPB ONs was assessed using an in vitro hemolysis assay. Notably, the RBCs incubated with a high dose of IHTPB ONs (400 μg/mL) still retained a negligible hemolysis rate (below 2%) (Figure S16). This indicates that IHTPB ONs exhibit good blood compatibility, suggesting their potential as a safe candidate for intravenous administration.

3.8 | In Vivo Biodistribution and NIR-Triggered Tumor Hyperthermia

In this study, a B16F10 tumor-bearing mouse model was established to evaluate the tumor-targeting capability of IHTPB ONs. Following tail-vein administration of free IR780, IHTPB ONs, or ITPB ONs, in vivo IR780 fluorescence in the mice was monitored using an IVIS system. At 24 h post-injection, the IHTPB ON and ITPB ON groups exhibited significantly stronger fluorescence signals in the tumor regions compared with the free IR780 group (Figure 7a,b), suggesting that these ONs effectively enhanced tumor accumulation of IR780 via the enhanced permeability and retention (EPR) effect. Moreover, the IHTPB ON group displayed significantly higher IR780 fluorescence intensity than the ITPB ON group. Consistently, ex vivo fluorescence imaging and quantitative analysis of tumors (Figure 7c,d) showed that the IHTPB ON-treated tumors exhibited the strongest IR780 signals among all groups. These results indicate that IHTPB ONs achieved superior tumor accumulation compared with ITPB ONs, benefiting from both the EPR effect and HA-mediated CD44 targeting. Furthermore, in both the IHTPB ON and ITPB ON groups, IR780 fluorescence signals in the liver and lungs were higher than those in the tumors, likely due to the inevitable uptake of these ONs by the mononuclear phagocyte system (MPS). In contrast, free IR780 molecules exhibited markedly lower accumulation in major organs and tumors, attributable to their rapid hepatic metabolism [57, 58]. To assess the hyperthermia-generating capability of IHTPB ONs accumulated in tumor tissues, B16F10 tumor-bearing mice were subjected to laser irradiation of the tumor region at 24 h post-injection, and the tumor temperature was monitored using an infrared thermal imaging camera. During irradiation, the IHTPB ON group exhibited a significantly greater increase in tumor temperature than both the ITPB ON and free IR780 groups (Figure 7e,f). These results indicate that tumor-targeted PB/IR780-mediated photothermal effects from IHTPB ONs enable efficient tumor heating. In contrast, the limited tumor accumulation and low photothermal conversion efficiency of free IR780 hinder effective temperature elevation within tumors.

To further improve tumor specificity and reduce MPS uptake, alternative administration strategies may be considered in future studies. In particular, local delivery approaches, such as intratumoral injection or localized depot systems (e.g., hydrogel-based or implantable formulations), may enhance tumor retention, prolong local exposure, and minimize systemic distribution. These strategies could be especially beneficial for melanoma phototherapy, where localized control of drug release and photothermal activation may further enhance therapeutic efficacy while reducing off-target accumulation.

3.9 | In Vivo Antitumor Potency

The in vivo antitumor efficacy of combined PTT and PDT mediated by IHTPB ONs was investigated in B16F10 tumor-bearing mice by monitoring tumor volume changes for up to 14 days after treatment (Figure 8a). As shown in Figure 8b, in the absence of laser irradiation, tumors in mice treated with IHTPB ONs grew rapidly and reached volumes comparable to those in the PBS group, indicating negligible cytotoxicity of the IHTPB ONs. This observation is consistent with the in vitro results presented in Figure 6d,e. In contrast, following laser irradiation, B16F10 tumor-bearing mice treated with free IR780, ITPB ONs, or IHTPB ONs showed pronounced tumor growth inhibition during the first 6 days post-treatment. However, tumors in the free IR780 and ITPB ON groups began to progressively regrow thereafter. Notably, under laser irradiation, treatment with IHTPB ONs resulted in sustained suppression of tumor growth throughout the entire observation period. Furthermore, mice receiving IHTPB ONs combined with laser irradiation exhibited significant tumor regression, as evidenced by an obvious reduction in tumor size (Figure S17). Consistent with the observed tumor growth inhibition, ex vivo analysis showed that tumors from mice treated with IHTPB ONs under laser irradiation exhibited the smallest size and lowest weight among all groups (Figure 8c,d). Notably, the survival rate of tumor-bearing mice receiving IHTPB ONs in combination with laser irradiation was significantly higher than that of the other treatment groups (Figure 8e). Collectively, these results demonstrate that IHTPB ONs combined with laser irradiation exert the most potent antitumor effect. In contrast, ITPB ONs displayed only limited antitumor efficacy due to the absence of HA-mediated tumor targeting. Moreover, the therapeutic effectiveness of free IR780 was constrained by poor tumor accumulation, pronounced photobleaching, and tumor hypoxia.

To further elucidate the antitumor mechanism, immunohistochemical analysis of tumor sections was performed. H&E staining revealed that treatment with IHTPB ONs under laser irradiation induced more extensive tumor tissue damage, including pronounced karyolysis, apoptosis, and necrosis, compared with the other groups (Figure 8f). In addition, tumors treated with IHTPB ONs combined with laser irradiation exhibited the lowest Ki-67

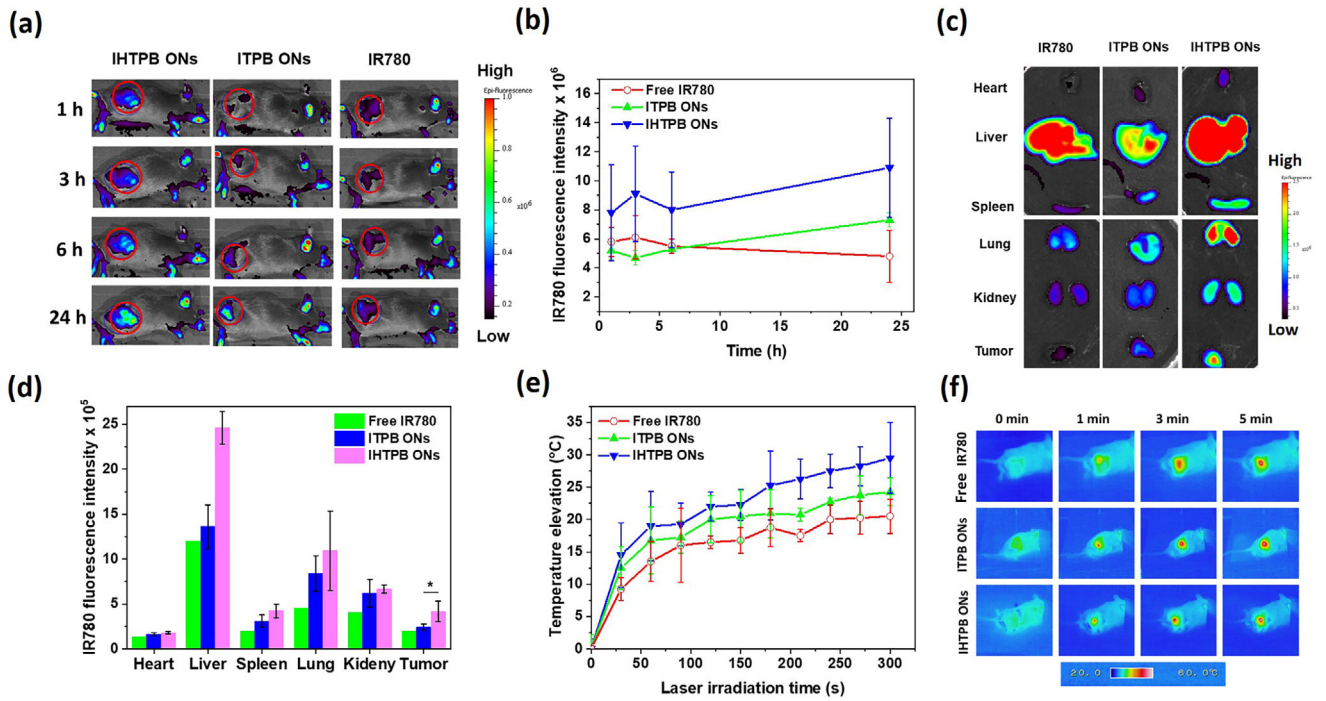

FIGURE 7 | (a) In vivo IR780 fluorescence images and (b) corresponding intensity quantification of B16F10 tumor-bearing mice intravenously injected with IR780, ITPB ONs, or IHTPB ONs ($n = 3$). Tumor sites are indicated by red circles. (c) Ex vivo IR780 fluorescence images and (d) fluorescence intensities of tumors and major organs collected 24 h post-injection ($n = 3$). (e) Temperature elevation curves ($n = 3$) and (f) thermal images of B16F10 tumor-bearing mice under NIR laser irradiation following different treatments.

expression, indicating a strong suppression of B16F10 cell proliferation. Notably, tumors treated with IHTPB ONs under laser irradiation exhibited a marked reduction in GPX4 expression compared with those receiving the same formulation without irradiation. Moreover, under laser irradiation, the IHTPB ON group displayed the lowest GPX4 staining among the free IR780 and ITPB ON groups, corresponding to significant intracellular GSH depletion of the IHTPB ONs + laser irradiation group (Figure 4c). These observations further suggest that the PB-mediated GSH oxidation combined with photothermal-enhanced TA-driven Michael addition achieved by tumor-targeting IHTPB ONs, may effectively deplete intracellular GSH, thereby suppressing GPX4 activity. Importantly, HIF-1α expression in tumor tissues treated with IHTPB ONs and laser irradiation was significantly reduced relative to that in other treatment groups, demonstrating effective alleviation of tumor hypoxia through PB-mediated O_2 production. These results are consistent with the in vitro findings on intracellular $^1O_2$ generation (Figure 4d,e). Collectively, these results demonstrate that tumor-targeting IHTPB ONs, featuring self-supplied O_2 generation and photothermal-enhanced GSH depletion, effectively maximize the synergistic antitumor efficacy of PTT and PDT, leading to pronounced inhibition of B16F10 tumor growth and prolonged survival of treated mice. Notably, the body weight of mice remained stable across all treatment groups (Figure S18), indicating the absence of severe acute toxicity. Furthermore, H&E staining of major organs, including the heart, liver, spleen, lung, and kidney, revealed no obvious histopathological abnormalities in any group (Figure S19). Through blood biochemistry tests, no significant changes were observed in ALT/AST/BUN/CRE concentrations in the tumor-bearing mice treated with IHTPB ONs and laser irradiation compared to the PBS group (Figure S20). These findings confirm that the therapeutic strategy did not induce significant systemic or organ-specific toxicity.

Although the present study demonstrated encouraging therapeutic efficacy and favorable short-term biosafety, several limitations should be mentioned. First, the in vivo therapeutic evaluation was performed using a relatively small number of animals, which may limit the statistical power of the findings. Second, the current biosafety assessment primarily focused on short-term observations, including blood compatibility, body weight changes, histopathological examination of major organs, and serum biochemical analyses. More comprehensive safety evaluations, such as long-term toxicity, hematological and immunological analyses, pharmacokinetic studies, and extended biodistribution assessments in larger animal cohorts, will be necessary before clinical translation. These investigations will further validate the safety profile and therapeutic potential of the developed IHTPB ONs.

4 | Conclusion

Unlike most PB nanoparticles functionalized solely with HA, the PB ONs developed in this work were surface-engineered with both TA and HA, enabling dual-mode GSH depletion and enhanced photothermal stability of the photosensitizer, thereby amplifying melanoma-targeted synergistic PTT/PDT therapy. Through the multiple interactions of IR780 with TPB ONs and covalent conjugation of HA-SH with TA-rich ON surfaces upon Michael addition, the IHTPB ONs were fabricated. The IHTPB ONs were characterized to have a uniform

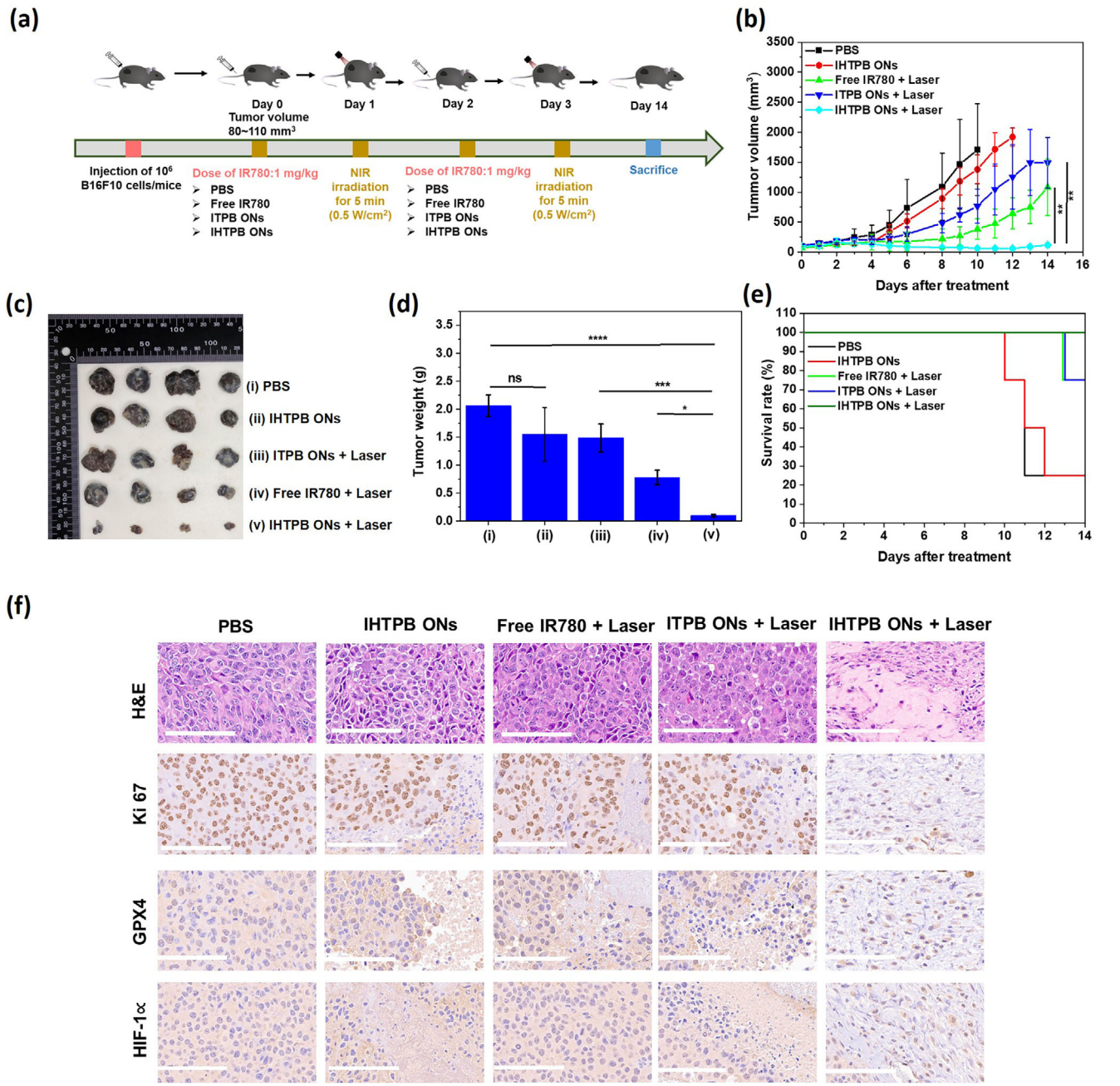

FIGURE 8 | (a) Schematic of the in vivo study evaluating B16F10 tumor growth inhibition. (b) Tumor volume changes in B16F10 tumor-bearing mice following different treatments ($n = 4$). (c) Photographs and (d) weights of tumors collected from euthanized mice after treatment ($n = 4$). (e) Survival curves of B16F10 tumor-bearing mice under various treatments ($n = 4$). (f) Representative H&E, Ki-67, GPX4, and HIF-1α staining of tumor sections from treated mice. Scale bars: 100 μm.

cubic shape, sound colloidal stability, and acidity/GSH-triggered IR780 liberation. Moreover, the IHTPB ONs exhibited prominent photothermal conversion efficiency (60%) via the combination of PB- and IR780-based photothermal effect, exerted PB/TA-mediated dual-mode GSH consumption and PB-facilitated O_2 production, and further produced abundant $^1O_2$ by the IR780-driven photodynamic effect. After being internalized by B16F10 melanoma cells through CD44-mediated endocytosis, the IHTPB ONs increased intracellular O_2 level, remarkably exhausted intracellular GSH, and produced both $^1O_2$ and hyperthermia under NIR laser irradiation, thus provoking apoptosis and ferroptosis via mitochondrial injury and LPO. More importantly, compared to free IR780 and ITPB ONs, the IHTPB ONs not only promoted tumor accumulation of IR780 via EPR effect and active CD44 targeting, but also potently inhibited melanoma growth and prolonged mouse survival through self-depleting GSH and self-producing O_2-enhanced PTT/PDT-mediated anticancer effects combined with ferroptosis. During IHTPB ON-mediated melanoma treatment, no significant adverse effects were observed. Collectively, these findings reveal a promising strategy for developing O_2 self-supplying and GSH-depleting nanocarriers capable of achieving tumor-targeted photosensitizer

delivery, thereby amplifying the therapeutic synergy of PTT and PDT against melanoma.

Author Contributions

Chia-Wei Kuo: investigation, methodology, visualization, formal analysis. **I-Ju Liu:** investigation, validation, visualization, formal analysis, methodology. **Wen-Hsuan Chiang:** investigation, funding acquisition, supervision, writing – original draft, writing – review and editing, methodology, conceptualization, data curation, resources. **Ju-An Liang:** investigation, formal analysis, methodology, visualization. **Chai-How Hsu:** formal analysis, investigation, methodology, validation, data curation, project administration, software. **Hsiang-Yun Chih:** investigation, visualization, formal analysis, methodology, software. **Tsai-Ching Hsu:** methodology, resources, investigation. **Bor-Show Tzang:** supervision, investigation, funding acquisition, resources, writing – original draft, project administration.

Acknowledgements

This work is supported by the National Science and Technology Council (NSTC 113-2628-E-005-002-MY3 and NSTC 113-2622-E-005-017), National Chung Hsing University, and Chung Shan Medical University (NCHU-CSMU 11401), Taiwan.

Funding

This work is supported by the National Science and Technology Council (NSTC 113-2628-E-005-002-MY3 and NSTC 113-2622-E-005-017), the National Chung Hsing University, and Chung Shan Medical University (NCHU-CSMU 11401), Taiwan.

Conflicts of Interest

The authors declare no conflicts of interest.

Data Availability Statement

The data that support the findings of this study are available from the corresponding author upon reasonable request.

References

1. C. Sun, Q. He, X. Yang, et al., "A Novel NIR-Dependent IDO-Inhibiting Ethosomes Treatment Melanoma Through PTT/PDT/Immunotherapy Synergy," *Colloids and Surfaces B: Biointerfaces* 251 (2025): 114565, https://doi.org/10.1016/j.colsurfb.2025.114565.

2. I. Lara-Vega and A. Vega-López, "Combinational Photodynamic and Photothermal-Based Therapies for Melanoma in Mouse Models," *Photodiagnosis and Photodynamic Therapy* 43 (2023): 103596, https://doi.org/10.1016/j.pdpdt.2023.103596.

3. S. M. Ostrowski and D. E. Fisher, "Biology of Melanoma," *Hematology/Oncology Clinics of North America* 35 (2021): 29–56, https://doi.org/10.1016/j.hoc.2020.08.010.

4. F. Bray, J. Ferlay, I. Soerjomataram, R. L. Siegel, L. A. Torre, and A. Jemal, "Global Cancer Statistics 2018: GLOBOCAN Estimates of Incidence and Mortality Worldwide for 36 Cancers in 185 Countries," *CA: A Cancer Journal for Clinicians* 68 (2018): 394–424.

5. J. Xie, R. Liang, Q. Li, et al., "Photosensitizer-Loaded Gold Nanocages for Immunogenic Phototherapy of Aggressive Melanoma," *Acta Biomaterialia* 142 (2022): 264–273, https://doi.org/10.1016/j.actbio.2022.01.051.

6. H. A. Tawbi, D. Schadendorf, E. J. Lipson, et al., "Relatlimab and Nivolumab Versus Nivolumab in Untreated Advanced Melanoma," *New England Journal of Medicine* 386 (2022): 24–34, https://doi.org/10.1056/NEJMoa2109970.

7. A. M. M. Eggermont, C. U. Blank, M. Mandala, et al., "Adjuvant Pembrolizumab Versus Placebo in Resected Stage III Melanoma," *New England Journal of Medicine* 378 (2018): 1789–1801, https://doi.org/10.1056/NEJMoa1802357.

8. L. Tagliaferri, V. Lancellotta, B. Fionda, et al., "Immunotherapy and Radiotherapy in Melanoma: A Multidisciplinary Comprehensive Review," *Human Vaccines & Immunotherapeutics* 18 (2022): 1903827, https://doi.org/10.1080/21645515.2021.1903827.

9. M. Wada-Ohno, T. Ito, and M. Furue, "Adjuvant Therapy for Melanoma," *Current Treatment Options in Oncology* 20 (2019): 63, https://doi.org/10.1007/s11864-019-0666-x.

10. A. Frazao, L. Rethacker, G. Jeudy, et al., "BRAF Inhibitor Resistance of Melanoma Cells Triggers Increased Susceptibility to Natural Killer Cell-Mediated Lysis," *Journal for ImmunoTherapy of Cancer* 8 (2020): 000275, https://doi.org/10.1136/jitc-2019-000275.

11. W. Hugo, J. M. Zaretsky, L. Sun, et al., "Genomic and Transcriptomic Features of Response to Anti-PD-1 Therapy in Metastatic Melanoma," *Cell* 165 (2016): 35–44, https://doi.org/10.1016/j.cell.2016.02.065.

12. G. Molina, G. G. Kasumova, M. Qadan, and G. M. Boland, "Use of Immunotherapy and Surgery for Stage IV Melanoma," *Cancer* 126 (2020): 2614–2624, https://doi.org/10.1002/cncr.32817.

13. J. Li, S. Wang, F. Fontana, et al., "Nanoparticles-Based Phototherapy Systems for Cancer Treatment: Current Status and Clinical Potential," *Bioactive Materials* 23 (2022): 471–507.

14. Z. Xie, T. Fan, J. An, et al., "Emerging Combination Strategies With Phototherapy in Cancer Nanomedicine," *Chemical Society Reviews* 49 (2020): 8065–8087, https://doi.org/10.1039/D0CS00215A.

15. D. Gao, X. Guo, X. Zhang, et al., "Multifunctional Phototheranostic Nanomedicine for Cancer Imaging and Treatment," *Materials Today Bio* 5 (2020): 100035, https://doi.org/10.1016/j.mtbio.2019.100035.

16. H. Y. Chih, I.-J. Liu, T. C. Lin, et al., "Tumor-Targeting Cu^{2+}/IR820-Rich Nanozymes to Exert Photothermal-Reinforced Reactive Oxygen Species Production and Dual Glutathione Scavenging for Synergistic Cancer Therapy," *Journal of Colloid and Interface Science* 703 (2026): 139183, https://doi.org/10.1016/j.jcis.2025.139183.

17. Y. Cai, T. Chai, W. Nguyen, et al., "Phototherapy in Cancer Treatment: Strategies and Challenges," *Signal Transduction and Targeted Therapy* 10 (2025): 115, https://doi.org/10.1038/s41392-025-02140-y.

18. I. Baldea and A. G. Filip, "Photodynamic Therapy in Melanoma–An Update," *Journal of Physiology and Pharmacology* 63 (2012): 109–118.

19. T. C. Lin, I.-J. Liu, H. Y. Chih, et al., "Photothermal-Enhanced ROS Storm by Hyaluronic Acid-Conjugated Nanocatalysts to Amplify Tumor-Specific Photo-Chemodynamic Therapy and Immune Response," *International Journal of Biological Macromolecules* 309 (2025): 142975, https://doi.org/10.1016/j.ijbiomac.2025.142975.

20. W. Cui, S. Zhu, X. Pan, W. Zhang, and T. Wang, "Gold(III) Porphyrin-Metal-Polyphenolic Nanocomplexes: Breaking Intracellular Redox Environment for Enhancing Mild-Temperature Photothermal Therapy," *ACS Applied Materials & Interfaces* 16 (2024): 30810–30818, https://doi.org/10.1021/acsami.4c04196.

21. K. F. Chu and D. E. Dupuy, "Thermal Ablation of Tumours: Biological Mechanisms and Advances in Therapy," *Nature Reviews Cancer* 14 (2014): 199–208, https://doi.org/10.1038/nrc3672.

22. Y. Zhong, X. Zhang, L. Yang, et al., "Hierarchical Dual-Responsive Cleavable Nanosystem for Synergetic Photodynamic/Photothermal Therapy Against Melanoma," *Materials Science and Engineering: C* 131 (2021): 112524, https://doi.org/10.1016/j.msec.2021.112524.

23. J. Yi, L. Liu, W. Gao, et al., "Advances and Perspectives in Phototherapy-Based Combination Therapy for Cancer Treatment," *Journal of Materials Chemistry B* 12 (2024): 6285–6304, https://doi.org/10.1039/D4TB00483C.

24. W. Li, J. Yang, L. Luo, et al., "Targeting Photodynamic and Photothermal Therapy to the Endoplasmic Reticulum Enhances Immunogenic

Cancer Cell Death," *Nature Communications* 10 (2019): 3349, https://doi.org/10.1038/s41467-019-11269-8.

25. H. Sun, Z. Fan, Q. Pei, Z. Xie, T. Zhang, and C. Ma, "Simple Porphyrin Nanoparticles for Combined Photo-Immunotherapy of Colorectal Cancer," *Biomaterials Advances* 178 (2026): 214466.

26. Z. Huang, H. Xu, A. D. Meyers, et al., "Photodynamic Therapy for Treatment of Solid Tumors—Potential and Technical Challenges," *Technology in Cancer Research & Treatment* 7 (2008): 309–320, https://doi.org/10.1177/153303460800700405.

27. X. Zhao, J. Liu, J. Fan, H. Chao, and X. Peng, "Recent Progress in Photosensitizers for Overcoming the Challenges of Photodynamic Therapy: From Molecular Design to Application," *Chemical Society Reviews* 50 (2021): 4185–4219, https://doi.org/10.1039/D0CS00173B.

28. D. Ma, W. Chen, L. Wang, R. Han, and K. Tang, "O_2 Self-Sufficient and Glutathione-Depleted Nanoplatform for Amplifying Phototherapy Synergistic Thermodynamic Therapy," *Colloids and Surfaces B: Biointerfaces* 222 (2023): 113060, https://doi.org/10.1016/j.colsurfb.2022.113060.

29. F. Shu, T. Yang, X. Zhang, et al., "Hyaluronic Acid Modified Covalent Organic Polymers for Efficient Targeted and Oxygen-Evolved Phototherapy," *Journal of Nanobiotechnology* 19 (2021): 4, https://doi.org/10.1186/s12951-020-00735-x.

30. S. Liu, Y. Wang, S. Yao, et al., "Combinative Dual-Nanoparticle Assembly Improves Oxygen-Autarky PDT Efficacy in Hypoxic Tumors," *Chemical Engineering Journal* 515 (2025): 163836, https://doi.org/10.1016/j.cej.2025.163836.

31. M. Tavakkoli Yaraki, B. Liu, and Y. Tan, "Emerging Strategies in Enhancing Singlet Oxygen Generation of Nano-Photosensitizers Toward Advanced Phototherapy," *Nano-Micro Letters* 14 (2022): 123, https://doi.org/10.1007/s40820-022-00856-y.

32. H. Y. Kwon, Y. Jung, H. Jeon, and H. S. Han, "Investigation Into Recent Advanced Strategies of Reactive Oxygen Species-Mediated Therapy Based on Prussian Blue: Conceptualization and Prospect," *Bioactive Materials* 48 (2025): 71.

33. B. Zhou, B. P. Jiang, W. Sun, et al., "Water-Dispersible Prussian Blue Hyaluronic Acid Nanocubes With Near-Infrared Photoinduced Singlet Oxygen Production and Photothermal Activities for Cancer Theranostics," *ACS Applied Materials & Interfaces* 10 (2018): 18036–18049, https://doi.org/10.1021/acsami.8b01387.

34. A. P. Mathew, S. K. Rajendrakumar, A. Mohapatra, et al., "Hyaluronan-Coated Prussian Blue Nanoparticles Relieve LPS-Induced Peritonitis by Suppressing Oxidative Species Generation in Tissue-Resident Macrophages," *Biomaterials Science* 10 (2022): 1248–1256, https://doi.org/10.1039/D1BM01796A.

35. W. Gao, Y. Wang, Y. Zheng, and X. Cai, "Prussian Blue Nanoparticle: From a Photothermal Conversion Agent and a Drug Delivery System, to a Bioactive Drug," *Accounts of Materials Research* 5 (2024): 687–698, https://doi.org/10.1021/accountsmr.3c00260.

36. M. A. Busquets and J. Estelrich, "Prussian Blue Nanoparticles: Synthesis, Surface Modification, and Biomedical Applications," *Drug Discovery Today* 25 (2020): 1431–1443, https://doi.org/10.1016/j.drudis.2020.05.014.

37. Prussian Blue Package Insert, Radiogardase®-Cs (Ferric Hexacyanoferrate), Heyl Chem.-pharm. Fabrik GmbH & Co. KG, Berlin, Germany (2007).

38. Y. H. Chen, I.-J. Liu, T. C. Lin, et al., "PEGylated Chitosan-Coated Nanophotosensitizers for Effective Cancer Treatment by Photothermal-Photodynamic Therapy Combined With Glutathione Depletion," *International Journal of Biological Macromolecules* 266 (2024): 131359, https://doi.org/10.1016/j.ijbiomac.2024.131359.

39. D. Wolny, M. Stojko, and A. Zajdel, "Novel Strategies of Glutathione Depletion in Photodynamic and Chemodynamic Therapy: A Review," *Advances in Clinical and Experimental Medicine* 34 (2025): 1213–1221, https://doi.org/10.17219/acem/191025.

40. J. Zou, Z. Li, Y. Zhu, et al., "pH/GSH Dual Responsive Nanosystem for Nitric Oxide Generation Enhanced Type I Photodynamic Therapy," *Bioactive Materials* 34 (2024): 414–421.

41. M. Ghasemian, F. Kazeminava, A. Naseri, et al., "Recent Progress in Tannic Acid Based Approaches as a Natural Polyphenolic Biomaterial for Cancer Therapy: A Review," *Biomedicine & Pharmacotherapy* 166 (2023): 115328, https://doi.org/10.1016/j.biopha.2023.115328.

42. M. Sahiner, S. S. Suner, and N. Sahiner, "Nanoparticles for Biomedical Use Derived From Natural Biomolecules: Tannic Acid and Arginine," *Biomedicines* 13 (2025): 209, https://doi.org/10.3390/biomedicines13010209.

43. C. T. Drucker, A. R. Cicali, A. M. P. Roberts, C. A. Hughey, and L. W. Senger, "Identification of Alkaline-Induced Thiolyl-Chlorogenic Acid Conjugates With Cysteine and Glutathione," *Food Chemistry* 423 (2023): 136267, https://doi.org/10.1016/j.foodchem.2023.136267.

44. W. Shao, Y. Yang, W. Shen, L. Ren, and P. Zhu, "Hyaluronic Acid-Conjugated Methotrexate and 5-Fluorouracil for Targeted Drug Delivery," *International Journal of Biological Macromolecules* 273 (2024): 132671, https://doi.org/10.1016/j.ijbiomac.2024.132671.

45. K. A. Liang, H. Y. Chih, I.-J. Liu, et al., "Tumor-Targeted Delivery of Hyaluronic Acid/Polydopamine-Coated Fe^{2+}-doped Nano-Scaled Metal–Organic Frameworks With Doxorubicin Payload for Glutathione Depletion-Amplified Chemodynamic-Chemo Cancer Therapy," *Journal of Colloid and Interface Science* 677 (2025): 400–415, https://doi.org/10.1016/j.jcis.2024.07.241.

46. M. H. Hsieh, T. H. Wang, S. H. Hu, et al., "Tumor Site-Specific PEG Detachment and Active Tumor Homing of Therapeutic PEGylated Chitosan/Folate-Decorated Polydopamine Nanoparticles to Augment Antitumor Efficacy of Photothermal/Chemo Combination Therapy," *Chemical Engineering Journal* 446 (2022): 137243, https://doi.org/10.1016/j.cej.2022.137243.

47. S. Yang, Y. Zhang, R. Chang, et al., "Versatile $Bi_2M_oO_6$/Prussian Blue-Au Nanoplatform for Oxygen-Self-Produced and GSH-Depleted Enhanced Sonodynamic Efficacy," *Journal of Colloid and Interface Science* 679 (2025): 929–938, https://doi.org/10.1016/j.jcis.2024.10.107.

48. C. Ren, Y. Cheng, W. Li, et al., "Ultra-Small Bi_2S_3 Nanodot-Doped Reversible Fe(ii/iii)-Based Hollow Mesoporous Prussian Blue Nanocubes for Amplified Tumor Oxidative Stress-Augmented Photo-/Radiotherapy," *Biomaterials Science* 8 (2020): 1981–1995, https://doi.org/10.1039/C9BM02014D.

49. H. Wang, R. Qu, Q. Chen, et al., "PEGylated Prussian Blue Nanoparticles for Modulating Polyethyleneimine Cytotoxicity and Attenuating Tumor Hypoxia for Dual-Enhanced Photodynamic Therapy," *Journal of Materials Chemistry B* 10 (2022): 5410–5421, https://doi.org/10.1039/D2TB00571A.

50. Y. Yang, S. Zhang, X. Hu, et al., "Oxygen-Driven Prussian Blue Nanomotor Promotes Cancer Immunotherapy by Disrupting Redox State-Induced Tumor Disulfide Death," *Journal of Colloid and Interface Science* 700 (2025): 138404, https://doi.org/10.1016/j.jcis.2025.138404.

51. C. Chen, H. Yang, X. Yang, and Q. Ma, "Tannic Acid: A Crosslinker Leading to Versatile Functional Polymeric Networks: A Review," *RSC Advances* 12 (2022): 7689–7711, https://doi.org/10.1039/D1RA07657D.

52. W. Li, S. Liu, Y. Zhang, et al., "Dual-Inhibition of Lactate Metabolism and Prussian Blue-Mediated Radical Generation for Enhanced Chemodynamic Therapy and Antimetastatic Effect," *Nanoscale* 15 (2023): 9214–9228, https://doi.org/10.1039/D3NR01052J.

53. T. Khan, R. Waseem, Z. Zehra, et al., "Mitochondrial Dysfunction: Pathophysiology and Mitochondria-Targeted Drug Delivery Approaches," *Pharmaceutics* 14 (2022): 2657, https://doi.org/10.3390/pharmaceutics14122657.

54. N. Kumar, W. Qian, and B. Van Houten, "Sick Mitochondria Cause Telomere Damage: Implications for Disease," *Molecular & Cellular Oncology* 7 (2019): 1678362, https://doi.org/10.1080/23723556.2019.1678362.

55. Y. Hou, Q. Fu, Y. Kuang, et al., "Unsaturated Fatty Acid-Tuned Assembly of Photosensitizers for Enhanced Photodynamic Therapy via Lipid Peroxidation," *Journal of Controlled Release* 334 (2021): 213–223, https://doi.org/10.1016/j.jconrel.2021.04.022.

56. F. A. Deng, M. Y. Yan, Y. B. Liu, et al., "Plasma Membrane-Targeted Photooxidant for Chemotherapy-Enhanced Lipid Peroxidation," *ACS Applied Bio Materials* 5 (2022): 4523–4530, https://doi.org/10.1021/acsabm.2c00597.

57. J. Lin, X. Cai, F. Zou, et al., "Fluorescent Nanoparticles Achieve Efficient Photothermal Conversion and Enhanced Antitumor Efficacy Through Intermolecular Aggregation-Caused Quenching," *Aggregate* 6 (2025): 723, https://doi.org/10.1002/agt2.723.

58. S. Y. Lin, R. Y. Huang, W. C. Liao, C. C. Chuang, and C. W. Chang, "Multifunctional PEGylated Albumin/IR780/Iron Oxide Nanocomplexes for Cancer Photothermal Therapy and MR Imaging," *Nanotheranostics* 2 (2018): 106–116, https://doi.org/10.7150/ntno.19379.

Supporting Information

Additional supporting information can be found online in the Supporting Information section.

Supporting File: adhm71596-sup-0001-SuppMat.docx.